
Swarm Reinforcement Learning for Adaptive Mesh Refinement

Niklas Freymuth^{1*} Philipp Dahlinger¹ Tobias Würth² Simon Reisch¹
Luise Kärger² Gerhard Neumann¹

¹Autonomous Learning Robots, Karlsruhe Institute of Technology, Karlsruhe

²Institute of Vehicle Systems Technology, Karlsruhe Institute of Technology, Karlsruhe

Abstract

The Finite Element Method, an important technique in engineering, is aided by Adaptive Mesh Refinement (AMR), which dynamically refines mesh regions to allow for a favorable trade-off between computational speed and simulation accuracy. Classical methods for AMR depend on task-specific heuristics or expensive error estimators, hindering their use for complex simulations. Recent learned AMR methods tackle these problems, but so far scale only to simple toy examples. We formulate AMR as a novel Adaptive Swarm Markov Decision Process in which a mesh is modeled as a system of simple collaborating agents that may split into multiple new agents. This framework allows for a spatial reward formulation that simplifies the credit assignment problem, which we combine with Message Passing Networks to propagate information between neighboring mesh elements. We experimentally validate the effectiveness of our approach, Adaptive Swarm Mesh Refinement (ASMR), showing that it learns reliable, scalable, and efficient refinement strategies on a set of challenging problems. Our approach significantly speeds up computation, achieving up to 30-fold improvement compared to uniform refinements in complex simulations. Additionally, we outperform learned baselines and achieve a refinement quality that is on par with a traditional error-based AMR strategy without expensive oracle information about the error signal.

1 Introduction

The Finite Element Method (FEM) is a widely used numerical technique in engineering and applied sciences for solving complex partial differential equations [1, 2, 3, 4]. The method discretizes the continuous problem domain into smaller, finite elements, allowing for an efficient numerical solution. A key aspect of the FEM for complex systems is AMR, which dynamically refines regions of high solution variability, allowing for a favorable trade-off between computational speed and simulation accuracy [5, 6, 7]. As problems in engineering grow more complex, the FEM and especially Adaptive Mesh Refinement (AMR) techniques have become increasingly important tools in providing reliable and precise solutions. Applications of AMR include fluid dynamics [8, 9, 10, 11, 12, 13], structural mechanics [14, 15, 16, 17], and astrophysics [18, 19, 20]. Yet, classical approaches for AMR usually rely on problem-dependent error indicators or require expensive error estimates [21, 22, 23, 24, 25, 12], making them cumbersome to use in practice.

To address this issue, we formalize AMR as a Reinforcement Learning (RL) [26] problem. Following previous work [27, 28, 29], we iteratively encode the state of the current simulation as local observations that we feed to RL agents, who then determine which elements of a mesh to refine. However, previous work has issues with scalability due to an expensive inference process [27], misaligned objectives and high variance in the state transitions [29], and noisy reward signals [28]. To mitigate

*correspondence to niklas.freymuth@kit.edu

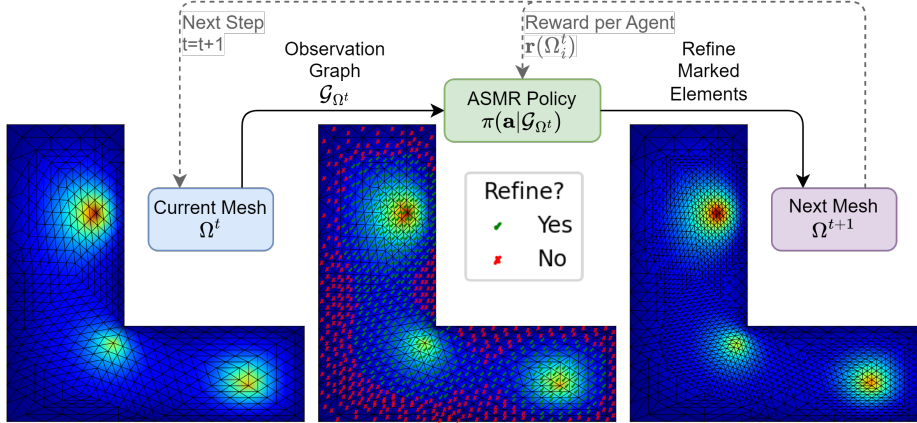


Figure 1: Given a mesh Ω^t , an observation graph \mathcal{G}_{Ω^t} encodes the elements as graph nodes and the neighborhood between elements as edges. The graph is given to a learned policy π , which marks mesh elements for refinement. A remesher refines the mesh, and spatial rewards $r(\Omega_i^t)$ are calculated for all agents i based on the quality of the refinement. This process is iterated for several steps until the mesh is fully refined.

these issues and scale to more complex problems, we formulate AMR as a Swarm RL [30, 31] problem, extending this framework to per-agent rewards, shared observations, and the option of splitting agents into new agents as required in the AMR process. We introduce a novel spatial reward formulation that provides a dense reward signal for the refinement of each mesh element, simplifying the credit assignment problem for swarm systems. Our policy is based on Message Passing Networks (MPNs) [32], a class of Graph Neural Networks (GNNs) [33, 34, 35, 36] that has proven to be effective for physical simulations [37, 38]. The resulting method, Adaptive Swarm Mesh Refinement (ASMR), consistently produces highly refined meshes with thousands of elements while applying to arbitrary Partial Differential Equations (PDEs). A high-level overview is given in Figure 1.

Experimentally, we show the effectiveness of our approach on a suite of challenging PDEs, including a non-stationary heat diffusion problem and a linear elasticity task. We implement our tasks in scikit-fem [39] as OpenAI gym [40] environments, using conforming triangular meshes and corresponding h-adaptive refinements [41, 42] for all experiments. Further, we implement and compare to current state-of-the-art RL methods for AMR [27, 28, 29]². We find that these methods struggle when confronted with finer meshes, while ASMR produces stable and consistent refinements across different tasks. To assess the efficacy of ASMR, we also compare it with a conventional error-based AMR heuristic that requires oracle information on the errors of each mesh element during inference. Our results show that ASMR yields comparable performance in most scenarios while being 2 to 30 times faster to compute than a uniform mesh. We conduct an extensive series of ablations to show which parts of the approach make it uniquely effective, finding that using spatial individual rewards per agent clearly outperforms a global reward signal for all agents.

To summarize our contributions, we (1) propose a novel Markov Decision Process (MDP) formulation that naturally integrates local rewards for swarms of agents that split agents into a set of new agents; (2) combine this formulation with MPNs and a novel spatial reward formulation to reliably and efficiently scale to meshes with thousands of elements; (3) demonstrate the effectiveness of our approach on a suite of challenging PDEs, outperforming current state-of-the-art RL methods and achieving comparable results to classical error-based AMR heuristics without requiring expensive error indicators during inference.

2 Related Work

Learned Physics Simulation. A considerable body of work deals with directly learning to simulate physical systems with neural networks. These approaches typically learn from data generated by

²We publish the first codebase on RL for AMR, including all methods and tasks presented in this paper, to facilitate research in this direction. The code is available at <https://github.com/NiklasFreymuth/ASMR>.

some underlying ground-truth simulator and train the network to predict the (change in) quantities of interest during a simulation. The main advantages of such learned physics simulators are that they are often orders of magnitude faster than their classical counterparts and that they are fully differentiable, lending them to use cases such as Inverse Design [43, 44, 45]. Researchers have developed simulators based on simple feed-forward networks [46, 47] and Convolutional Neural Networks [48, 49, 50, 51, 52, 53, 54, 55, 56]. Closely related to our method are Graph Network Simulators (GNSs) [32, 37, 57, 58, 59, 60, 38, 61], which utilize GNNs to encode physical problems as a graph on which to compute quantities of interest per node. Here, a recent method [62] jointly learns a GNS and an AMR strategy on mesh edges to allow for simulation on different resolutions.

Physics-Informed Neural Networks [63, 64, 65] are mesh-free methods designed to directly train neural networks to satisfy the governing equations of a physical system. They share the goal of using deep neural networks to solve PDEs, yet differ in their approach in that they directly approximate the equations rather than providing a mesh for a classical solver. Thus, AMR strategies provide a more robust, flexible, and risk-averse approach to solving complex physics problems that demand high precision and accuracy [11, 66, 13]. As Physics-Informed Neural Networks also operate on geometric domains, they have been extended to GNNs architectures [67, 68, 69].

Supervised Learning for AMR. Applications of supervised learning for AMR include directly calculating an error per mesh element with a Multilayer Perceptron (MLP) [11] and predicting mesh densities from domain images [66]. Additionally, recurrent networks have been used to find optimal marking strategies for second-order elliptical PDEs [70]. Another body of work speeds up the computation of Dual Weighted Residual [71, 72] error estimators by substituting expensive parts of the procedure with neural networks. Here, recent methods [73, 74] consider learning a metric tensor from solution information that can then be used in existing refinement procedures [23]. Other approaches employ neural networks to solve the strong form of the adjoint problem and use hand-crafted features to compute error estimates [75, 13] directly. We leverage the fact that RL can optimize non-differentiable rewards, enabling us to directly learn a refinement strategy.

Reinforcement Learning for AMR. Current research in Reinforcement Learning for AMR involves various approaches, such as optimizing the positions of mesh elements [76], predicting a global threshold for heuristic-based refinement using existing error estimates [77], and generating quadrilateral meshes by iteratively extracting elements from the problem domain [78].

We instead directly manipulate the mesh elements themselves. This approach presents a unique challenge in that the observation and action spaces are in constant flux as the mesh is adapted. While existing methods in this direction typically derive their observation spaces from the mesh geometry and the solution computed on the mesh, the main difference lies in how they deal with this problem. One suggested solution [27] is to treat the entire mesh as an action and observation space for a single agent. The agent provides an action for each element using a policy based on GNNs and refines the *Argmax* of the elements. This method demands solving the system of equations after each refinement step, significantly increasing inference time while reducing the amount of information per environment sample. Another approach [29] iteratively selects a random element during training and uses an MLP policy to determine its marking based on local and global features. During inference, the method performs a *Sweep* for all mesh elements in parallel. This procedure speeds up the inference but causes a misalignment in the environment transition between training and inference [28]. Additionally, during training, the agent 'jumps around' after each action, causing consecutive states to be only weakly correlated, which leads to high variance in the state transitions.

The most similar method to ours is Value Decomposition Graph Networks (*VDGN*) [28] which frames AMR as a cooperative multi-agent problem by setting a maximum refinement depth and creating a Markov game from the bounded number of maximum agents. *VDGN* employs a Value Decomposition Network [79] to circumvent the posthumous credit assignment problem [80] of vanishing agents. Despite the efficiency of the method's refinement during training and inference, its overall quality is compromised if the value decomposition of individual elements is subpar. Thus, it performs well on simple tasks with few refinement steps but struggles for finer meshes. In summary, none of the existing RL methods fully utilize the spatial nature of AMR and thus only scale to either simple examples or comparatively shallow refinements. We instead formulate AMR as a Swarm Reinforcement Learning problem with spatial rewards, allowing us to naturally deal with the problem of changing observation and action spaces while also providing a strong feedback signal to all agents.

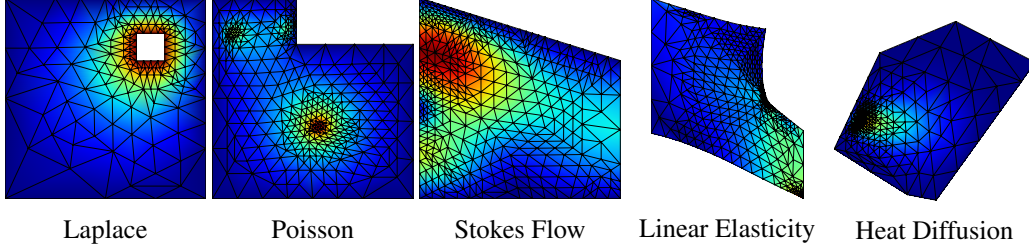


Figure 2: Visualizations of refinements provided by ASMR on different tasks. The heatmap in the background represents the respective quantities of interest. ASMR provides accurate refinements for a large range of systems of equations. From left to right: The Laplace equation requires refinement near the inner boundary, which represents a heat source. For the Poisson equation, a multi-modal load function causes multiple regions of interest that need to be taken into account. The Stokes flow uses more complex shape functions to solve the system of equations, and requires high precision near the inlet on the left boundary. For the linear elasticity task, we consider the deformation and the resulting stress as quantities of interest. The heat diffusion task has a moving heat source and thus requires accurate refinements on the path of the heat source to predict an accurate solution of the final step.

3 Adaptive Swarm Mesh Refinement

In the following, we introduce the individual components of ASMR, including our novel Adaptive Swarm Markov Decision Process (ASMDP) and spatial reward function. We consider each element $\Omega_i^t \subseteq \Omega^t$ of a mesh Ω^t to be an agent in a swarm system. The agent’s state is its position in the mesh, as well as boundary conditions and other PDE-dependent quantities. The agent’s observation consists of a local view of a graph \mathcal{G}_{Ω^t} where each node represents a mesh element and each edge the neighborhood of two elements. Our approach trains an MPN-based policy $\pi(\mathbf{a}|\mathcal{G}_{\Omega^t})$ that computes a joint action vector $\mathbf{a} \in \mathcal{A}^N$ for each element of the mesh by passing messages along the observation graph. Details for the MPN are provided in Appendix A. The action vector is used for refinement, and the process is iteratively repeated for the refined mesh for a given number of steps. Since our policy uses a GNN, it is equivariant to permutation and can handle varying numbers of agents by construction. Figure 1 provides a schematic overview.

Adaptive Swarm Markov Decision Process. We frame AMR as an instance of a Swarm Markov Decision Process (SwarMDP) [30, 31], which can be seen as a special case of a decentralized partially observable MDP for swarm systems. For AMR, we extend the process to per-agent rewards, shared observations, and adaptive numbers of agents. Formally, we define an ASMDP as a tuple $\langle \mathbb{S}, \mathbb{O}, \mathbb{A}, T, \mathbf{r}, \xi, \mathbf{M} \rangle$. Here, \mathbb{A} is the action space for the system of agents, \mathbb{S} is the state space of the complete system, and \mathbb{O} is the space of observations for this state space. Let $\mathcal{S}^N \subset \mathbb{S}$, $\mathcal{O}^N \subset \mathbb{O}$, $\mathcal{A}^N \subset \mathbb{A}$ denote the subsets of the state, observation, and action spaces with exactly $N \in \mathbb{N}$ agents. The transition function $T : \mathcal{S}^N \times \mathcal{A}^N \rightarrow \mathcal{S}^K$ maps to a new system state with a potentially different number $K \neq N$ of agents, and $\mathbf{r} : \mathcal{S}^N \times \mathcal{A}^N \rightarrow \mathbb{R}^N$ is a per-agent reward function. The observation graph of the agents is calculated from their states via the observation function $\xi : \mathcal{S}^N \rightarrow \mathcal{O}^N$. To accommodate changing numbers of agents throughout an episode, we define an agent mapping $\mathbf{M}^t \in [0, 1]^{N \times K}$ with $\forall_j \sum_i \mathbf{M}_{ij}^t = 1$ that specifies how agents evolve at time step t . Each entry \mathbf{M}_{ij}^t describes whether agent i at step t progresses into agent j at step $t + 1$. The influence of each agent at step t on the reward, in terms of all successor agents it is responsible for up to step $t + k$, can then be computed as $\mathbf{M}^{t,k} := \mathbf{M}^t \mathbf{M}^{t+1} \dots \mathbf{M}^{t+k-1}$.

Given a policy $\pi : \mathcal{O}^n \times \mathcal{A}^n \rightarrow [0, 1]$, the usual objective in RL is to maximize the return, i.e., the expected discounted cumulative future reward $J^t = \mathbb{E}_\pi \left[\sum_{k=0}^{\infty} \gamma^k r^{t+k} \right]$ for the reward r^{t+k} at step $t + k$. Adapting this to varying numbers of agents within a single episode, as necessary for e.g., the refinement of mesh elements, yields

$$J_i^t := \mathbb{E}_\pi \left[\sum_{k=0}^{\infty} \gamma^k (\mathbf{M}^{t,k} \mathbf{r}^{t+k})_i \right] \quad (1)$$

for agent i at step t . Intuitively, this return represents the discounted sum of rewards of all agents that agent i is responsible for. For training e.g., a value function, we set $V(\mathcal{G}_{\Omega^t}, i) = \mathbf{r}(\Omega_i^t) + \gamma \sum_j \mathbf{M}_{ij}^t V(\mathcal{G}_{\Omega^{t+1}}, j)$. The targets for Q -functions are derived analogously.

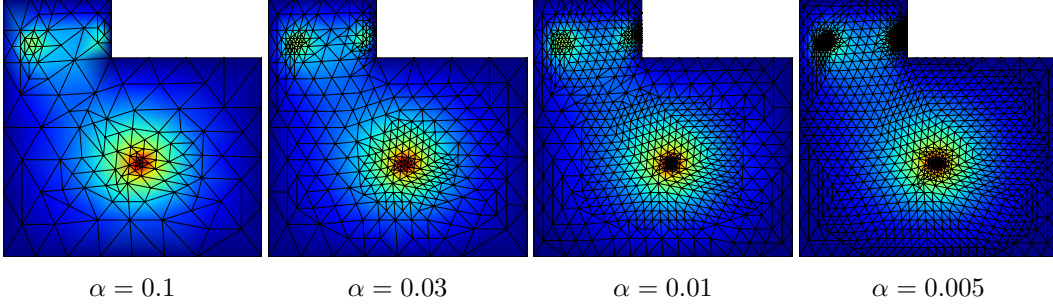


Figure 3: Visualizations of the final refinements of ASMR on a Poisson problem for different values of the element penalty α . All refinements focus on the relevant parts of the problem, and lower element penalties lead to more fine-grained meshes.

Agents and Observations. Given a domain Ω and a mesh $\Omega^t := \{\Omega_i^t \subseteq \Omega \mid \bigcup_i \Omega_i^t = \Omega\}$, we view each mesh element Ω_i^t as an agent. Each element’s action space comprises a binary decision to mark it for refinement. These markings are provided to a remesher, which refines all marked elements, yielding a finer mesh $\Omega^{t+1} = \{\Omega_j^{t+1}\}_j$. Here, $\Omega_j^{t+1} := \Omega_i^t$ for no refinement and $\Omega_j^{t+1} \subsetneq \Omega_i^t$ with $\bigcup_j \Omega_j^{t+1} = \Omega_i^t$ if Ω_i^t is refined. The remesher may also refine unmarked elements to assert a conforming solution [41], i.e., to make sure that elements of the mesh align with each other at the boundaries and interfaces to ensure continuity of solution variables between adjacent elements. We define the mapping for an agent to its successor agents as the indicator function $\mathbf{M}_{ij}^t := \mathbb{I}(\Omega_j^{t+1} \subseteq \Omega_i^t)$. I.e., an agent maps to all future agents that it spawns, or equivalently, an element is responsible for all sub-elements that it refines into over time. While we focus on mesh refinement in this work, this mapping can be extended to coarsening by setting e.g. $\mathbf{M}_{ij}^t := \mathbb{I}(\Omega_j^{t+1} \subseteq \Omega_i^t) + (\mathbb{I}(\Omega_i^t \subsetneq \Omega_j^{t+1}) / (\sum_k \mathbb{I}(\Omega_k^t \subsetneq \Omega_j^{t+1})))$.

For encoding the observations, we use an *observation graph* $\mathcal{G}_{\Omega^t} = \mathcal{G} = (\mathcal{V}, \mathcal{E}, \mathbf{X}_{\mathcal{V}}, \mathbf{X}_{\mathcal{E}}, \mathbf{g})$, which is a bidirectional directed graph with nodes \mathcal{V} and edges $\mathcal{E} \subseteq \mathcal{V} \times \mathcal{V}$. The symbols $\mathbf{X}_{\mathcal{V}} : \mathcal{V} \rightarrow \mathbb{R}^{d_{\mathcal{V}}}$ and $\mathbf{X}_{\mathcal{E}} : \mathcal{E} \rightarrow \mathbb{R}^{d_{\mathcal{E}}}$ denote PDE-specific node and edge features of dimensions $d_{\mathcal{V}}$ and $d_{\mathcal{E}}$ respectively, and $\mathbf{g} \in \mathbb{R}^{d_{\mathbf{g}}}$ are global features. Details are given in Appendix B.

Reward. A good refinement strategy trades off the accuracy of the solution of the mesh Ω^t with its total number of elements $|\Omega_i^t| \in \Omega^t$. We define an error per element as the difference in the solution of this element compared to a solution using a fine-grained reference mesh Ω^* [27]. We consider Ω^* to be optimal, but very slow to compute due to a large number of elements. However, we only require the reference mesh Ω^* for the reward calculation, not during inference. For each element Ω_i^t we then integrate over the evaluated differences of all midpoints $p_{\Omega_m^*} \in \Omega_m^*$ of reference elements Ω_m^* that fall into it, scaling each by the area $\text{Area}(\Omega_m^*)$ of its respective element. This procedure results in an error estimate

$$\text{err}(\Omega_i^t) \approx \sum_{\Omega_m^* \subseteq \Omega_i^t} \text{Area}(\Omega_m^*) |u_{\Omega^*}(p_{\Omega_m^*}) - u_{\Omega^t}(p_{\Omega_m^*})|, \quad (2)$$

where u_{Ω^*} denotes the solution on the fine mesh and u_{Ω^t} the solution on the current mesh. We note that this error estimate can be efficiently calculated using a k -d tree [81] and that it is generally applicable for a large range of PDEs. Problem-specific error estimates may be used instead to include domain knowledge. To get an error estimate that is consistent across different geometries, we normalize the error with the total error of the elements of the initial mesh Ω^0 , i.e., $\text{err}(\Omega_i^t) = \text{err}(\Omega_i^t) / \sum_{\Omega_j^0 \subseteq \Omega^0} \text{err}(\Omega_j^0)$. We then formulate a local reward per element as

$$\mathbf{r}(\Omega_i^t) := \frac{1}{\text{Area}(\Omega_i^t)} \left(\text{err}(\Omega_i^t) - \sum_j \mathbf{M}_{ij}^t \text{err}(\Omega_j^{t+1}) \right) - \alpha \left(\sum_j \mathbf{M}_{ij}^t - 1 \right), \quad (3)$$

where α is a hyperparameter that penalizes adding new elements.

This reward function evaluates whether a refinement decreases the overall error by enough to justify the extra resources required, with a reward of 0 for unrefined elements. By incorporating a novel area scaling term, the policy is encouraged to focus on smaller elements with a relatively high potential

reduction in error rather than larger elements with a low average error reduction, up to some threshold depending on the element penalty α . Optimizing this reward thus corresponds to refining elements with a high reduction in *error per area* rather than a high decrease in *absolute error*, since the area scaling term effectively cancels out the area of the integration points in Equation 2. We find that the combination of a local formulation and the area scaling term allows for a simpler credit assignment for the RL agents, as it ensures that each agent gets rewarded for its own actions and that rewards of elements of different sizes are on the same scale. The policies optimized on this reward implicitly minimize the maximum remaining error of the mesh, while also making sure that the mean error stays sufficiently low. We compare this to directly minimizing the maximum error in Appendix C.2.

Since the effects of mesh refinement can be non-local for elliptical PDEs, we optimize the average of the local and global returns, i.e.,

$$J_i^{t'} = \frac{1}{2}J_i^t + \frac{1}{2}J^t, \quad (4)$$

where J_i^t is the return of agent i at step t as shown in Equation 1, and J^t is the global return calculated using the average reward $r = \frac{1}{N} \sum_j r_j$. In multi-quantity systems of equations, it is important for the mesh to be suitable for all the quantities of interest. For this, we calculate individual errors $\text{err}^d(\Omega_i^t)$ for each solution dimension and then use a weighted sum of these as the overall error.

4 Experiments

Setup. All learned methods are trained on 100 PDEs and their corresponding initial and reference meshes Ω^0, Ω^* to limit the number of required reference meshes during training. We experiment with 10 different target mesh resolutions per method to produce a wide range of solutions, as detailed in Appendix E.3. We repeat each experiment for 10 random seeds and report the average performance on 100 randomly sampled but fixed evaluation PDEs for each seed. These PDEs are disjoint from the training PDEs, and both sets of PDEs consist of randomly sampled domains as well as boundary and initial conditions as detailed below. Details on the setup and the computational budget for our experiments are provided in Appendix C.1. The reference mesh Ω^* is created by uniformly refining the initial mesh 6 times. An environment episode consists of drawing one of the 100 training PDE without replacement, and iteratively refining the coarse initial mesh Ω^0 a total of $T = 6$ times unless mentioned otherwise. We experiment with both on- and off-policy RL algorithms for our method. More concretely, we choose Deep Q-Network (DQN) [82, 83] and Proximal Policy Optimization (PPO) [84] with discrete actions due to their simplicity and empirical success.

We measure the quality of the created meshes by comparing them to the fine-grained reference Ω^* . In practical applications, it is often critical for the AMR strategy to minimize the maximum remaining error while also keeping the mean error low. Since the maximum remaining error can not easily be evaluated and is susceptible to outliers, we approximate it as the average of the Top 0.1% of errors of all integration points $p_{\Omega_m^*}$. For comparability across PDEs, we normalize the resulting value by the error of the initial mesh Ω^0 . We discuss and evaluate the mean remaining error as an additional metric in Appendix D.6. Appendix E.1 lists all further algorithm and network training hyperparameters.

Graph Features. The features \mathbf{X}_v of each node $v \in \mathcal{V}$ are given as the element area, the distance to the closest boundary, and the mean and standard deviation of the solution on the element’s vertices. Edge features $\mathbf{X}_\mathcal{E}$ are defined as Euclidean distances between element midpoints. We omit absolute positions to ensure that the observations are equivariant under the Euclidean group [37, 36] to utilize the underlying symmetry of the task. The global features \mathbf{g} consist of the number of mesh elements and mesh nodes, as well as the current environment step. We use additional task-dependent global and node features for all considered systems of equations, as described in Appendix B.

Systems of Equations We experiment on various 2D elliptical PDEs, namely the Laplace equation, the Poisson equation, a Stokes flow task, a linear elasticity example, and a non-stationary heat diffusion equation. The domains are L-shapes, rectangles with a square hole, trapezoids, and convex polygons. Figure 2 provides examples of refinements of ASMR on all tasks. The PDEs and the FEM are implemented using *scikit-fem* [39], and we use conforming triangular meshes and linear elements unless mentioned otherwise. The code provides OpenAI gym [40] environments for all tasks. We define the systems of equations and their specific features in Appendix B.

Baselines. We adapt several recent RL methods for AMR as baselines [27, 28, 29]. We use our error estimates as the basis of all reward calculations for comparability but otherwise calculate the rewards

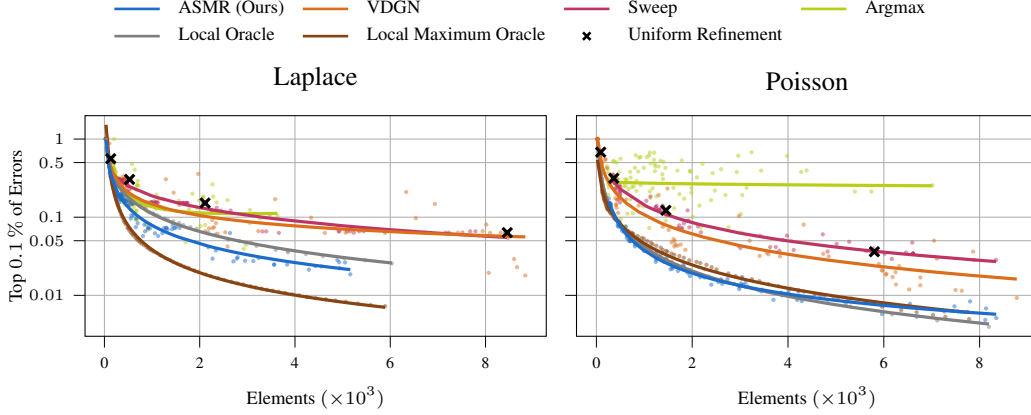


Figure 4: Pareto plot of normalized Top 0.1 % of errors and number of final mesh elements for (Left) Laplace’s Equation and (Right) Poisson’s Equation. For Laplace’s Equation, all methods provide reasonable refinements on different mesh resolutions. For Poisson’s Equation, which uses a multi-modal load function, *Argmax* fails to provide meaningful refinements, while *Sweep* does not improve over uniform refinements. We removed sporadic outliers above 9000 elements from *VDGN* to enhance visibility. Overall, ASMR is significantly more stable than the other learned methods, and produces more consistent and higher-quality refinements, especially for finer meshes.

as described in the respective papers. *Argmax* [27] considers a single agent that predicts a continuous action for each mesh element and always marks the element with the highest action for refinement. *Sweep* [29] trains a single-agent policy by randomly sampling an element on the mesh and deciding its refinement on local features and a global resource budget. During inference, each timestep consists of a sweep over all elements, during which each element may be marked. Finally, *VDGN* [28] uses Value Decomposition Networks [79] to assign a value for each agent from a global reward. As there is no Q-function for the PPO version of *VDGN*, we instead decompose the value function as the sum of value functions of the individual elements. We use an MPN policy for *Argmax* and *VDGN*, while the single-agent *Sweep* utilizes a simple MLP. Detailed hyperparameters and further details for the baselines are provided in Appendix E.2

We also compare to a traditional error-based *Local Oracle* heuristic [85, 86, 29]. Given a refinement threshold θ , the *Local Oracle* iteratively refines all elements Ω_i^t for which $\text{err}(\Omega_i^t) > \theta \cdot \max_j \text{err}(\Omega_j^t)$. As we are interested in the reduction of the maximum error, we analogously define the *Local Maximum Oracle*, which uses the maximum error per element $\max_{\Omega_m^* \subseteq \Omega_i^t} |u_{\Omega^*}(p_{\Omega_m^*}) - u_{\Omega^t}(p_{\Omega_m^*})|$ as a surrogate error estimate. Note that these baselines require the fine-grained reference mesh Ω^* , which is usually unavailable during inference as it is expensive to compute. The heuristics act locally and greedy and can thus lead to sub-optimal refinements for globally propagating errors, which is a well-known issue for elliptic PDEs [87, 29]. In contrast, RL methods learn to maximize an expected return, allowing them to find more holistic refinement strategies.

Ablations. To determine which parts of ASMR make it uniquely effective, we conduct a series of ablation experiments. We look at both the area scaling and the spatial decomposition of our reward, as well as an alternate reward formulation that uses the maximum error per element instead of its average as described in Appendix C.2. Further, we ablate different node features and the number of training PDEs that are used and experiment with PPO and DQN as the RL backbones.

5 Results

Quantitative Results. For all baselines, we experiment with both PPO and DQN as the RL backbone on the Laplace equation in Appendix D.1. While *Argmax* works better with DQN, both *VDGN* and *Sweep* produce better results with PPO. Similarly, Appendix D.2 shows that ASMR works better with PPO. For each method, we use the better of the two algorithms in all other experiments.

Using the experiments on the RL backbone, Figure 4 compares the different approaches on Laplace’s equation (Left) and Poisson’s equation (Right). Each point visualizes the mean performance of a single policy evaluated on 100 evaluation environments. The lines are a log-log quadratic regression over

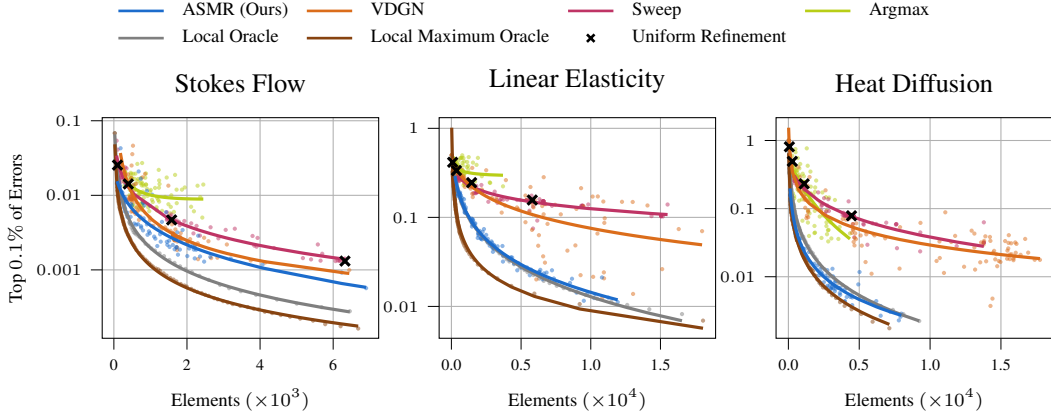


Figure 5: Pareto plot of normalized Top 0.1 % of errors and the number of final mesh elements for (Left) the Stokes flow, (Middle) the linear elasticity task, and (Right) the non-stationary heat diffusion equations. ASMR provides accurate refinements, outperforming the learned baselines and performing on par with the oracle heuristics on both the linear elasticity and the heat diffusion tasks. However, the local oracles outperform all RL methods on the Stokes flow task, presumably because the task displays high solution variability both near the inlet and along the flow boundaries.

the aggregated results of each method. ASMR discovers efficient refinement strategies, outperforming the learned baselines, especially for finer meshes. Notably, ASMR also outperforms the *Local Oracle* on the Laplace task and the *Local Maximum Oracle* on the Poisson equation without access to the true error information. These results indicate the effectiveness of our Swarm RL framework for learning non-greedy refinement strategies that minimize error throughout the entire environment episode. Figure 5 provides results on the remaining tasks. The results are consistent with that of Figure 3. ASMR again outperforms all learned baselines and is competitive with the error-based heuristics on both the linear elasticity and the heat diffusion task. Yet, the local heuristics perform better than the RL methods on the Stokes flow task, likely because the task requires both high precision near the inlet and a consistent refinement level across the whole domain. Appendix D.6 provides results for the mean remaining error as an additional evaluation metric on all tasks, showing that ASMR generally outperforms the other learned methods and is competitive with the local heuristics on this metric.

Qualitative Results. Figure 2 shows refinements of ASMR on randomly sampled systems of equations for all considered tasks. The refinement strategy adapts to the given task, providing an efficient trade-off between simulation accuracy and the number of elements used. Figure 3 visualizes the refinements of ASMR on randomly sampled domains and load functions for Poisson’s Equation. ASMR suggests refinements of different granularity depending on the element penalty α , yet always focuses on the modes of the load function $f(x)$ and the interior edge of the L shape. Appendix F provides additional visualizations for our method on all tasks (c.f., Appendix F.1) and for all methods on the Poisson task (c.f., Appendix F.2). Appendix F.3 additionally shows the iterative marking procedure of our approach on an exemplary Poisson PDE.

Ablations and Practical Considerations. The reward proposed in Equation 3 crucially features an area scaling per element and a spatial allocation of the decrease in error to the individual mesh elements. Figure 6 individually and collectively ablates these decisions. We find that the combination of both features is unique responsible for the effectiveness of our method. The spatial reward’s limited expressiveness is compensated by area scaling. However, the area scaling can only be leveraged if it is allocated to individual mesh elements, as it may introduce excessive reward noise on the full mesh. The maximum reward variant of Appendix C.2 explicitly minimizes the maximum error of the mesh. Both rewards show similar performance. The maximum error works well on the Top 0.1 % error metric, while Equation 3 tends to be better on the mean remaining error of the mesh.

We evaluate the effect of different parameters for the target mesh resolution in Appendix D.5, finding that ASMR provides meshes with considerably more consistent numbers of elements for a given target resolution than the other learned methods. Further ablation results are provided in Appendix D.2.

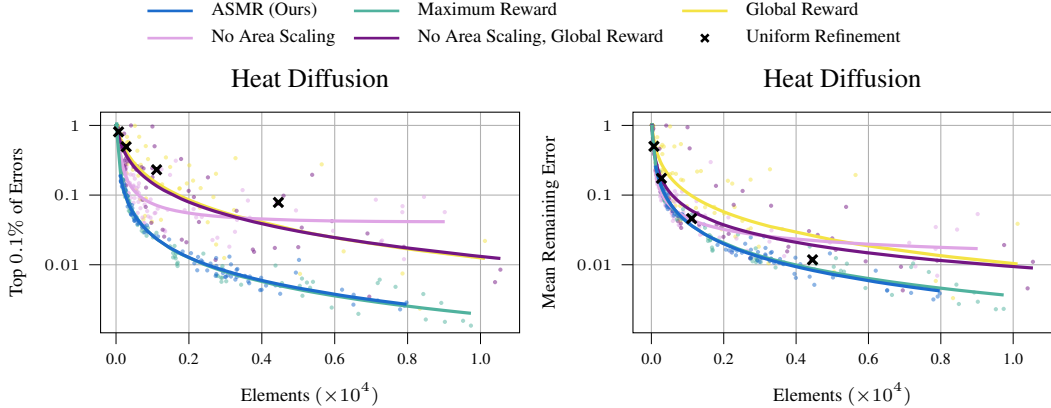


Figure 6: Pareto plot of different reward function ablations of (Left) normalized Top 0.1 % of errors and (Right) normalized mean remaining error compared to the number of final mesh elements. Our method benefits from both the area scaling term of Equation 3 and a spatial reward formulation. The alternate maximum reward of Appendix C.2 is similar to that of Equation 3. It performs slightly better for the Top 0.1 % of errors, but is slightly worse on the mean remaining error.

Here, we find that 100 training PDEs are sufficient and that adding absolute positions in the node features is detrimental, while the solution information and the load function improve the performance.

Appendix D.3 compares the wall-clock time of ASMR with that of the reference Ω^* , showing that our approach provides a significant speedup over a uniform refinement for all tasks. On the Stokes flow task, we achieve a speedup of more than factor 30 due to the comparatively expensive P_1/P_2 Taylor-Hood-elements [88]. Appendix D.4 shows that our approach exhibits exceptional generalization across various domains and load functions for Poisson’s equation. This ability is likely a by-product of the MPN architecture and the used observation graphs, as both facilitate generalization by training refinement strategies based on local neighborhoods rather than global meshes.

6 Conclusion

We present ASMR, a novel method for Adaptive Mesh Refinement that uses Swarm Reinforcement Learning to iteratively refine meshes for efficient solutions of Partial Differential Equations. Our approach treats mesh elements as a swarm system and trains a shared policy for all agents using Graph Neural Networks and a novel per-agent reward formulation. Our method yields stable and efficient refinements for meshes with thousands of elements without requiring an error estimate during inference. The experiments demonstrate that ASMR outperforms existing Reinforcement Learning-based methods and achieves a refinement quality comparable to a traditional error-based refinement strategy that has access to an expensive oracle error signal. Further, our method generalizes well across different problem domains and PDEs and improves the computation speed in comparison to uniform refinements by a factor of 2 to 30.

Broader Impact Our proposed Adaptive Mesh Refinement technique can positively impact various fields relying on computational modeling and simulation. By reducing simulation times while maintaining high precision, this technology enables researchers to explore a wider range of scenarios. However, like any powerful tool, there are potential negative impacts, such as the development of advanced weapon models or exploitation of resources.

Limitations and Future Work Our approach solves the partial differential equation after each refinement step, which, while faster than uniform refinement, still requires a considerable amount of computation time. In future work, we will explore using Swarm RL for refinement strategies from just the raw geometry and boundary conditions of different systems of equations, potentially leading to even faster computations. Further, this work only considers 2D problems with triangular elements on comparatively simple domains. Here, we want to extend and modify our approach to quadrilateral meshes and more complex 3-dimensional domains.

Acknowledgments and Disclosure of Funding

NF was supported by the BMBF project Davis (Datengetriebene Vernetzung für die ingenieurtechnische Simulation). This work is also part of the DFG AI Resarch Unit 5339 regarding the combination of physics-based simulation with AI-based methodologies for the fast maturation of manufacturing processes. The financial support by German Research Foundation (DFG, Deutsche Forschungsgemeinschaft) is gratefully acknowledged. The authors acknowledge support by the state of Baden-Württemberg through bwHPC, as well as the HoreKa supercomputer funded by the Ministry of Science, Research and the Arts Baden-Württemberg and by the German Federal Ministry of Education and Research.

References

- [1] Susanne C Brenner and L Ridgway Scott. *The mathematical theory of finite element methods*, volume 3. Springer, 2008.
- [2] Junuthula Narasimha Reddy and David K Gartling. *The finite element method in heat transfer and fluid dynamics*. CRC press, 2010.
- [3] Junuthula Narasimha Reddy. *Introduction to the finite element method*. McGraw-Hill Education, 2019.
- [4] Robert Anderson, Julian Andrej, Andrew Barker, Jamie Bramwell, Jean-Sylvain Camier, Jakub Cerveny, Veselin Dobrev, Yohann Dudouit, Aaron Fisher, Tzanio Kolev, et al. Mfem: A modular finite element methods library. *Computers & Mathematics with Applications*, 81:42–74, 2021.
- [5] Tomasz Plewa, Timur Linde, V Gregory Weirs, et al. *Adaptive mesh refinement-theory and applications*. Springer, 2005.
- [6] Weizhang Huang and Robert D Russell. *Adaptive moving mesh methods*, volume 174. Springer Science & Business Media, 2010.
- [7] Krzysztof J Fidkowski and David L Darmofal. Review of output-based error estimation and mesh adaptation in computational fluid dynamics. *AIAA journal*, 49(4):673–694, 2011.
- [8] Marsha J Berger and Phillip Colella. Local adaptive mesh refinement for shock hydrodynamics. *Journal of computational Physics*, 82(1):64–84, 1989.
- [9] Timothy J Baker. Mesh adaptation strategies for problems in fluid dynamics. *Finite Elements in Analysis and Design*, 25(3-4):243–273, 1997.
- [10] Raunak Borker, Daniel Huang, Sebastian Grimberg, Charbel Farhat, Philip Avery, and Jason Rabinovitch. Mesh adaptation framework for embedded boundary methods for computational fluid dynamics and fluid-structure interaction. *International Journal for Numerical Methods in Fluids*, 90(8):389–424, 2019.
- [11] Zheyang Zhang, Yongxing Wang, Peter K Jimack, and He Wang. Meshingnet: A new mesh generation method based on deep learning. In *Computational Science–ICCS 2020: 20th International Conference, Amsterdam, The Netherlands, June 3–5, 2020, Proceedings, Part III 20*, pages 186–198. Springer, 2020.
- [12] Joseph Gregory Wallwork. *Mesh adaptation and adjoint methods for finite element coastal ocean modelling*. PhD thesis, Imperial College London, 2021.
- [13] Joseph Gregory Wallwork, Jingyi Lu, Mingrui Zhang, and Matthew D Piggott. E2n: Error estimation networks for goal-oriented mesh adaptation. *arXiv preprint arXiv:2207.11233*, 2022.
- [14] M Ortiz and JJ Quigley Iv. Adaptive mesh refinement in strain localization problems. *Computer Methods in Applied Mechanics and Engineering*, 90(1-3):781–804, 1991.
- [15] Nikolas Provatas, Nigel Goldenfeld, and Jonathan Dantzig. Efficient computation of dendritic microstructures using adaptive mesh refinement. *Physical Review Letters*, 80(15):3308, 1998.
- [16] Erwin Stein. *Adaptive finite elements in linear and nonlinear solid and structural mechanics*, volume 416. Springer Science & Business Media, 2007.

- [17] Gaël Gibert, Benoit Prabel, Anthony Gravouil, and Clémentine Jacquemoud. A 3d automatic mesh refinement x-fem approach for fatigue crack propagation. *Finite Elements in Analysis and Design*, 157:21–37, 2019.
- [18] Andrew J Cunningham, Adam Frank, Peggy Varnière, Sorin Mitran, and Thomas W Jones. Simulating magnetohydrodynamical flow with constrained transport and adaptive mesh refinement: algorithms and tests of the astrobear code. *The Astrophysical Journal Supplement Series*, 182(2):519, 2009.
- [19] Greg L Bryan, Michael L Norman, Brian W O’Shea, Tom Abel, John H Wise, Matthew J Turk, Daniel R Reynolds, David C Collins, Peng Wang, Samuel W Skillman, et al. Enzo: An adaptive mesh refinement code for astrophysics. *The Astrophysical Journal Supplement Series*, 211(2):19, 2014.
- [20] Thomas Guillet, Rüdiger Pakmor, Volker Springel, Praveen Chandrashekar, and Christian Klingenberg. High-order magnetohydrodynamics for astrophysics with an adaptive mesh refinement discontinuous galerkin scheme. *Monthly Notices of the Royal Astronomical Society*, 485(3):4209–4246, 2019.
- [21] Arup Mukherjee. *An adaptive finite element code for elliptic boundary value problems in three dimensions with applications in numerical relativity*. The Pennsylvania State University, 1996.
- [22] Eisuke Kita and Norio Kamiya. Error estimation and adaptive mesh refinement in boundary element method, an overview. *Engineering Analysis with Boundary Elements*, 25(7):479–495, 2001.
- [23] Masayuki Yano and David L Darmofal. An optimization-based framework for anisotropic simplex mesh adaptation. *Journal of Computational Physics*, 231(22):7626–7649, 2012.
- [24] Wolfgang Bangerth and Rolf Rannacher. *Adaptive Finite Element Methods for Differential Equations*. Birkhäuser, 2013.
- [25] Jakub Cerveny, Veselin Dobrev, and Tzanio Kolev. Nonconforming mesh refinement for high-order finite elements. *SIAM Journal on Scientific Computing*, 41(4):C367–C392, 2019.
- [26] Richard S Sutton and Andrew G Barto. *Reinforcement learning: An introduction*. MIT press, 2018.
- [27] Jiachen Yang, Tarik Dzanic, Brenden K Petersen, Jun Kudo, Ketan Mittal, Vladimir Tomov, Jean-Sylvain Camier, Tuo Zhao, Hongyuan Zha, Tzanio Kolev, Robert Anderson, and Daniel Faissol. Reinforcement learning for adaptive mesh refinement. *26th International Conference on Artificial Intelligence and Statistics (AISTATS)*, 2023.
- [28] Jiachen Yang, Ketan Mittal, Tarik Dzanic, Socratis Petrides, Brendan Keith, Brenden Petersen, Daniel Faissol, and Robert Anderson. Multi-agent reinforcement learning for adaptive mesh refinement. *22nd International Conference on Autonomous Agents and Multiagent Systems (AAMAS)*, 2023.
- [29] Corbin Foucart, Aaron Charous, and Pierre FJ Lermusiaux. Deep reinforcement learning for adaptive mesh refinement. *arXiv preprint arXiv:2209.12351*, 2022.
- [30] Adrian Šošić, Wasiur R KhudaBukhsh, Abdelhak M Zoubir, and Heinz Koepl. Inverse reinforcement learning in swarm systems. In *Proceedings of the 16th Conference on Autonomous Agents and MultiAgent Systems*, pages 1413–1421, 2017.
- [31] Maximilian Hüttenrauch, Šošić Adrian, and Gerhard Neumann. Deep reinforcement learning for swarm systems. *Journal of Machine Learning Research*, 20(54):1–31, 2019.
- [32] Alvaro Sanchez-Gonzalez, Jonathan Godwin, Tobias Pfaff, Rex Ying, Jure Leskovec, and Peter Battaglia. Learning to simulate complex physics with graph networks. In *Proceedings of the 37th International Conference on Machine Learning*, pages 8459–8468. PMLR, 2020.
- [33] Franco Scarselli, Marco Gori, Ah Chung Tsoi, Markus Hagenbuchner, and Gabriele Monfardini. The graph neural network model. *IEEE Transactions on Neural Networks*, 20(1):61–80, 2009.
- [34] Peter W Battaglia, Jessica B Hamrick, Victor Bapst, Alvaro Sanchez-Gonzalez, Vinicius Zambaldi, Mateusz Malinowski, Andrea Tacchetti, David Raposo, Adam Santoro, Ryan Faulkner, et al. Relational inductive biases, deep learning, and graph networks. *arXiv preprint arXiv:1806.01261*, 2018.

- [35] Zonghan Wu, Shirui Pan, Fengwen Chen, Guodong Long, Chengqi Zhang, and S Yu Philip. A comprehensive survey on graph neural networks. *IEEE transactions on neural networks and learning systems*, 32(1):4–24, 2020.
- [36] Michael M Bronstein, Joan Bruna, Taco Cohen, and Petar Veličković. Geometric deep learning: Grids, groups, graphs, geodesics, and gauges. *arXiv preprint arXiv:2104.13478*, 2021.
- [37] Tobias Pfaff, Meire Fortunato, Alvaro Sanchez-Gonzalez, and Peter W. Battaglia. Learning mesh-based simulation with graph networks. In *International Conference on Learning Representations*, 2021.
- [38] Jonas Linkerhägner, Niklas Freymuth, Paul Maria Scheickl, Franziska Mathis-Ullrich, and Gerhard Neumann. Grounding graph network simulators using physical sensor observations. In *The Eleventh International Conference on Learning Representations (ICLR)*, 2023.
- [39] Tom Gustafsson and Geordie Drummond Mcbain. scikit-fem: A python package for finite element assembly. *Journal of Open Source Software*, 5(52):2369, 2020.
- [40] Greg Brockman, Vicki Cheung, Ludwig Pettersson, Jonas Schneider, John Schulman, Jie Tang, and Wojciech Zaremba. Openai gym. *arXiv preprint arXiv:1606.01540*, 2016.
- [41] Douglas N Arnold, Arup Mukherjee, and Luc Pouly. Locally adapted tetrahedral meshes using bisection. *SIAM Journal on Scientific Computing*, 22(2):431–448, 2000.
- [42] Rob Stevenson. The completion of locally refined simplicial partitions created by bisection. *Mathematics of computation*, 77(261):227–241, 2008.
- [43] Pierre Baqué, Edoardo Remelli, François Fleuret, and Pascal Fua. Geodesic convolutional shape optimization. In Jennifer G. Dy and Andreas Krause, editors, *Proceedings of the 35th International Conference on Machine Learning, ICML 2018, Stockholmsmässan, Stockholm, Sweden, July 10-15, 2018*, volume 80 of *Proceedings of Machine Learning Research*, pages 481–490. PMLR, 2018.
- [44] Nikita Durasov, Artem Lukoyanov, Jonathan Donier, and Pascal Fua. Debosh: Deep bayesian shape optimization. *arXiv preprint arXiv:2109.13337*, 2021.
- [45] Kelsey R Allen, Tatiana Lopez-Guevara, Kimberly Stachenfeld, Alvaro Sanchez-Gonzalez, Peter Battaglia, Jessica Hamrick, and Tobias Pfaff. Physical design using differentiable learned simulators. *arXiv preprint arXiv:2202.00728*, 2022.
- [46] Kiwon Um, Xiangyu Hu, and Nils Thuerey. Liquid splash modeling with neural networks. *Computer Graphics Forum*, 37(8):171–182, 2018.
- [47] Steffen Wiewel, Moritz Becher, and Nils Thuerey. Latent Space Physics: Towards Learning the Temporal Evolution of Fluid Flow. *Computer Graphics Forum*, 2019.
- [48] Xiaoxiao Guo, Wei Li, and Francesco Iorio. Convolutional neural networks for steady flow approximation. In *Proceedings of the 22nd ACM SIGKDD International Conference on Knowledge Discovery and Data Mining, KDD '16*, page 481–490, New York, NY, USA, 2016. Association for Computing Machinery.
- [49] Mengyu Chu and Nils Thuerey. Data-driven synthesis of smoke flows with cnn-based feature descriptors. *ACM Trans. Graph.*, 36(4), jul 2017.
- [50] You Xie, Erik Franz, Mengyu Chu, and Nils Thuerey. tempoGAN: A Temporally Coherent, Volumetric GAN for Super-resolution Fluid Flow. *ACM Transactions on Graphics (TOG)*, 37(4):95, 2018.
- [51] Yao Zhang, Woong Je Sung, and Dimitri N. Mavris. Application of convolutional neural network to predict airfoil lift coefficient. In *2018 AIAA/ASCE/AHS/ASC Structures, Structural Dynamics, and Materials Conference*, 2018.
- [52] Clemens Zimmerling, Daniel Trippe, Benedikt Fengler, and Luise Kärger. An approach for rapid prediction of textile draping results for variable composite component geometries using deep neural networks. *AIP Conference Proceedings*, 2113(1), 07 2019. 020007.
- [53] Byungsoo Kim, Vinicius C. Azevedo, Nils Thuerey, Theodore Kim, Markus Gross, and Barbara Solenthaler. Deep Fluids: A Generative Network for Parameterized Fluid Simulations. *Computer Graphics Forum (Proc. Eurographics)*, 38(2), 2019.

- [54] Saakaar Bhatnagar, Yaser Afshar, Shaowu Pan, Karthik Duraisamy, and Shailendra Kaushik. Prediction of aerodynamic flow fields using convolutional neural networks. *Computational Mechanics*, 64(2):525–545, jun 2019.
- [55] Benjamin Ummenhofer, Lukas Prantl, Nils Thuerey, and Vladlen Koltun. Lagrangian fluid simulation with continuous convolutions. In *International Conference on Learning Representations*, 2020.
- [56] Clemens Zimmerling, Christian Poppe, Oliver Stein, and Luise Kärger. Optimisation of manufacturing process parameters for variable component geometries using reinforcement learning. *Materials & Design*, 214:110423, 2022.
- [57] Zehang Weng, Fabian Paus, Anastasiia Varava, Hang Yin, Tamim Asfour, and Danica Kragic. Graph-based task-specific prediction models for interactions between deformable and rigid objects. In *2021 IEEE/RSJ International Conference on Intelligent Robots and Systems (IROS)*, pages 5741–5748, 2021.
- [58] Xu Han, Han Gao, Tobias Pfaff, Jian-Xun Wang, and Li-Ping Liu. Predicting physics in mesh-reduced space with temporal attention. *CoRR*, abs/2201.09113, 2022.
- [59] Meire Fortunato, Tobias Pfaff, Peter Wirmsberger, Alexander Pritzel, and Peter Battaglia. Multiscale meshgraphnets. In *ICML 2022 2nd AI for Science Workshop*, 2022.
- [60] Kelsey R Allen, Tatiana Lopez Guevara, Yulia Rubanova, Kimberly Stachenfeld, Alvaro Sanchez-Gonzalez, Peter Battaglia, and Tobias Pfaff. Graph network simulators can learn discontinuous, rigid contact dynamics. *Conference on Robot Learning (CoRL)*, 2022.
- [61] Kelsey R Allen, Yulia Rubanova, Tatiana Lopez-Guevara, William Whitney, Alvaro Sanchez-Gonzalez, Peter Battaglia, and Tobias Pfaff. Learning rigid dynamics with face interaction graph networks. *The Eleventh International Conference on Learning Representations (ICLR)*, 2023.
- [62] Tailin Wu, Takashi Maruyama, Qingqing Zhao, Gordon Wetzstein, and Jure Leskovec. Learning controllable adaptive simulation for multi-resolution physics. In *The Eleventh International Conference on Learning Representations*, 2023.
- [63] Maziar Raissi, Paris Perdikaris, and George E Karniadakis. Physics-informed neural networks: A deep learning framework for solving forward and inverse problems involving nonlinear partial differential equations. *Journal of Computational physics*, 378:686–707, 2019.
- [64] Shengze Cai, Zhiping Mao, Zhicheng Wang, Minglang Yin, and George Em Karniadakis. Physics-informed neural networks (pinns) for fluid mechanics: A review. *Acta Mechanica Sinica*, 37(12):1727–1738, 2021.
- [65] Anonymous. Physics-informed neural networks for data-free surrogate modelling and engineering optimization - an example from composite manufacturing. *Submitted to Materials & Design*, 2023.
- [66] Keefe Huang, Moritz Krügener, Alistair Brown, Friedrich Menhorn, Hans-Joachim Bungartz, and Dirk Hartmann. Machine learning-based optimal mesh generation in computational fluid dynamics. *arXiv preprint arXiv:2102.12923*, 2021.
- [67] Balthazar Donon, Zhengying Liu, Wenzhuo LIU, Isabelle Guyon, Antoine Marot, and Marc Schoenauer. Deep statistical solvers. In H. Larochelle, M. Ranzato, R. Hadsell, M.F. Balcan, and H. Lin, editors, *Advances in Neural Information Processing Systems*, volume 33, pages 7910–7921. Curran Associates, Inc., 2020.
- [68] Han Gao, Matthew J Zahr, and Jian-Xun Wang. Physics-informed graph neural galerkin networks: A unified framework for solving pde-governed forward and inverse problems. *Computer Methods in Applied Mechanics and Engineering*, 390:114502, 2022.
- [69] Masanobu Horie and NAOTO MITSUME. Physics-embedded neural networks: Graph neural pde solvers with mixed boundary conditions. In S. Koyejo, S. Mohamed, A. Agarwal, D. Belgrave, K. Cho, and A. Oh, editors, *Advances in Neural Information Processing Systems*, volume 35, pages 23218–23229. Curran Associates, Inc., 2022.
- [70] Jan Bohn and Michael Feischl. Recurrent neural networks as optimal mesh refinement strategies. *Computers & Mathematics with Applications*, 97:61–76, 2021.
- [71] Roland Becker and Rolf Rannacher. *Weighted a posteriori error control in FE methods*. IWR, 1996.

- [72] Roland Becker and Rolf Rannacher. An optimal control approach to a posteriori error estimation in finite element methods. *Acta numerica*, 10:1–102, 2001.
- [73] Krzysztof J Fidkowski and Guodong Chen. Metric-based, goal-oriented mesh adaptation using machine learning. *Journal of Computational Physics*, 426:109957, 2021.
- [74] Guodong Chen and Krzysztof J Fidkowski. Output-based adaptive aerodynamic simulations using convolutional neural networks. *Computers & Fluids*, 223:104947, 2021.
- [75] Julian Roth, Max Schröder, and Thomas Wick. Neural network guided adjoint computations in dual weighted residual error estimation. *SN Applied Sciences*, 4(2):62, 2022.
- [76] Filipe De Avila Belbute-Peres, Thomas Economon, and Zico Kolter. Combining differentiable pde solvers and graph neural networks for fluid flow prediction. In *international conference on machine learning*, pages 2402–2411. PMLR, 2020.
- [77] Andrew Gillette, Brendan Keith, and Socratis Petrides. Learning robust marking policies for adaptive mesh refinement. *arXiv preprint arXiv:2207.06339*, 2022.
- [78] Jie Pan, Jingwei Huang, Gengdong Cheng, and Yong Zeng. Reinforcement learning for automatic quadrilateral mesh generation: A soft actor–critic approach. *Neural Networks*, 157:288–304, 2023.
- [79] Peter Sunehag, Guy Lever, Audrunas Gruslys, Wojciech Marian Czarnecki, Vinicius Zambaldi, Max Jaderberg, Marc Lanctot, Nicolas Sonnerat, Joel Z Leibo, Karl Tuyls, et al. Value-decomposition networks for cooperative multi-agent learning. *arXiv preprint arXiv:1706.05296*, 2017.
- [80] Andrew Cohen, Ervin Teng, Vincent-Pierre Berges, Ruo-Ping Dong, Hunter Henry, Marwan Mattar, Alexander Zook, and Sujoy Ganguly. On the use and misuse of absorbing states in multi-agent reinforcement learning. *arXiv preprint arXiv:2111.05992*, 2021.
- [81] Jon Louis Bentley. Multidimensional binary search trees used for associative searching. *Communications of the ACM*, 18(9):509–517, 1975.
- [82] Volodymyr Mnih, Koray Kavukcuoglu, David Silver, Alex Graves, Ioannis Antonoglou, Daan Wierstra, and Martin Riedmiller. Playing atari with deep reinforcement learning. *arXiv preprint arXiv:1312.5602*, 2013.
- [83] Volodymyr Mnih, Koray Kavukcuoglu, David Silver, Andrei A Rusu, Joel Veness, Marc G Bellemare, Alex Graves, Martin Riedmiller, Andreas K Fidjeland, Georg Ostrovski, et al. Human-level control through deep reinforcement learning. *nature*, 518(7540):529–533, 2015.
- [84] John Schulman, Filip Wolski, Prafulla Dhariwal, Alec Radford, and Oleg Klimov. Proximal policy optimization algorithms. *arXiv preprint arXiv:1707.06347*, 2017.
- [85] Peter Binev, Wolfgang Dahmen, and Ron DeVore. Adaptive finite element methods with convergence rates. *Numerische Mathematik*, 97:219–268, 2004.
- [86] Wolfgang Bangerth, Carsten Burstedde, Timo Heister, and Martin Kronbichler. Algorithms and data structures for massively parallel generic adaptive finite element codes. *ACM Transactions on Mathematical Software (TOMS)*, 38(2):1–28, 2012.
- [87] Walter A Strauss. *Partial differential equations: An introduction*. John Wiley & Sons, 2007.
- [88] Volker John et al. *Finite element methods for incompressible flow problems*, volume 51. Springer, 2016.
- [89] Alfio Quarteroni and Silvia Quarteroni. *Numerical models for differential problems*, volume 2. Springer, 2009.
- [90] Olek C Zienkiewicz, Robert Leroy Taylor, and Jian Z Zhu. *The finite element method: its basis and fundamentals*. Elsevier, 2005.
- [91] Marcin Andrychowicz, Anton Raichuk, Piotr Stańczyk, Manu Orsini, Sertan Girgin, Raphaël Marinier, Leonard Hussenot, Matthieu Geist, Olivier Pietquin, Marcin Michalski, Sylvain Gelly, and Olivier Bachem. What matters for on-policy deep actor-critic methods? a large-scale study. In *International Conference on Learning Representations*, 2021.
- [92] John Schulman, Philipp Moritz, Sergey Levine, Michael Jordan, and Pieter Abbeel. High-dimensional continuous control using generalized advantage estimation. *arXiv preprint arXiv:1506.02438*, 2015.

- [93] Matteo Hessel, Joseph Modayil, Hado Van Hasselt, Tom Schaul, Georg Ostrovski, Will Dabney, Dan Horgan, Bilal Piot, Mohammad Azar, and David Silver. Rainbow: Combining improvements in deep reinforcement learning. In *Proceedings of the AAAI conference on artificial intelligence*, volume 32, 2018.
- [94] Hado Van Hasselt, Arthur Guez, and David Silver. Deep reinforcement learning with double q-learning. In *Proceedings of the AAAI conference on artificial intelligence*, volume 30, 2016.
- [95] Ziyu Wang, Tom Schaul, Matteo Hessel, Hado Hasselt, Marc Lanctot, and Nando Freitas. Dueling network architectures for deep reinforcement learning. In *International conference on machine learning*, pages 1995–2003. PMLR, 2016.
- [96] Tom Schaul, John Quan, Ioannis Antonoglou, and David Silver. Prioritized experience replay. In Yoshua Bengio and Yann LeCun, editors, *4th International Conference on Learning Representations, ICLR 2016, San Juan, Puerto Rico, May 2-4, 2016, Conference Track Proceedings*, 2016.
- [97] Adam Paszke, Sam Gross, Francisco Massa, Adam Lerer, James Bradbury, Gregory Chanan, Trevor Killeen, Zeming Lin, Natalia Gimelshein, Luca Antiga, et al. Pytorch: An imperative style, high-performance deep learning library. *Advances in neural information processing systems*, 32, 2019.
- [98] Diederik P Kingma and Jimmy Ba. Adam: A method for stochastic optimization. *arXiv preprint arXiv:1412.6980*, 2014.
- [99] Jimmy Lei Ba, Jamie Ryan Kiros, and Geoffrey E Hinton. Layer normalization. *stat*, 1050:21, 2016.
- [100] Kaiming He, Xiangyu Zhang, Shaoqing Ren, and Jian Sun. Deep residual learning for image recognition. In *Proceedings of the IEEE conference on computer vision and pattern recognition*, pages 770–778, 2016.

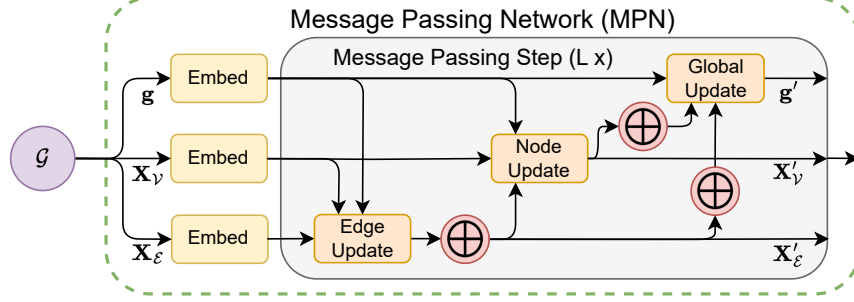


Figure 7: Detailed schematic of the MPN architecture employed by ASMR. Given a graph \mathcal{G} , the global features \mathbf{g} , node features $\mathbf{X}_{\mathcal{V}}$, and edge features $\mathbf{X}_{\mathcal{E}}$ are linearly embedded into separate latent spaces. From here, L message passing steps are performed. The resulting latent features per node are interpreted as a local observation encoding and can be given to an RL policy or value function.

A Message Passing Network Architecture

Given a graph $\mathcal{G} = (\mathcal{V}, \mathcal{E}, \mathbf{X}_{\mathcal{V}}, \mathbf{X}_{\mathcal{E}}, \mathbf{g})$, Message Passing Networks (MPN) [32, 37, 38] are GNN consisting of L *Message Passing Steps*. Each step l receives the output of the previous step and updates the features $\mathbf{X}_{\mathcal{V}}$, $\mathbf{X}_{\mathcal{E}}$ for all nodes $v \in \mathcal{V}$ and edges $e \in \mathcal{E}$, as well as globals \mathbf{g} . Using linear embeddings \mathbf{x}_v^0 , \mathbf{x}_e^0 , and \mathbf{g}^0 of the initial node, edge, and global features, the l -th step is given as

$$\mathbf{x}_e^{l+1} = f_{\mathcal{E}}^l(\mathbf{x}_v^l, \mathbf{x}_u^l, \mathbf{x}_e^l, \mathbf{g}^l), \text{ with } e = (u, v),$$

$$\mathbf{x}_v^{l+1} = f_{\mathcal{V}}^l(\mathbf{x}_v^l, \bigoplus_{e=(v,u) \in \mathcal{E}} \mathbf{x}_e^{l+1}, \mathbf{g}^l), \quad \text{and} \quad \mathbf{g}^{l+1} = f_{\mathbf{g}}^l(\bigoplus_{v \in \mathcal{V}} \mathbf{x}_v^{l+1}, \bigoplus_{e \in \mathcal{E}} \mathbf{x}_e^{l+1}, \mathbf{g}^l).$$

The operator \bigoplus is a permutation-invariant aggregation such as a sum, max, or mean operator. Each f^l is a learned function that we generally parameterize as a simple MLP. The network's final output is a learned representation \mathbf{x}_v^L for each node $v \in \mathcal{V}$. Figure 7 provides a schematic overview of the full MPN architecture.

B Systems of Equations

In its most general form, the FEM is used to approximate the solution $\mathbf{u}(\mathbf{x})$ for the set of test functions \mathbf{v} , which satisfies the weak formulation $\forall \mathbf{x} : \forall \mathbf{v}(\mathbf{x}) : a(\mathbf{u}(\mathbf{x}), \mathbf{v}(\mathbf{x})) = l(\mathbf{v}(\mathbf{x}))$ of the underlying system of equations. In the following, we describe the specific equations and boundary conditions used for our experiments.

B.1 Laplace's Equation

Let Ω be a domain with an inner boundary $\partial\Omega_0$ and an outer boundary $\partial\Omega_1$. We seek a solution $u(\mathbf{x})$ that satisfies the weak formulation of the Laplace Equation

$$\int_{\Omega} \nabla u(\mathbf{x}) \cdot \nabla v(\mathbf{x}) \, d\mathbf{x} = 0$$

for all test functions $v(\mathbf{x})$. Additionally, the solution has to satisfy the Dirichlet boundary conditions

$$u(\mathbf{x}) = 0, \mathbf{x} \in \partial\Omega_0 \quad \text{and} \quad u(\mathbf{x}) = 1, \mathbf{x} \in \partial\Omega_1.$$

We use a unit square $(0, 1)^2$ for the outer boundary $\partial\Omega_0$ of the domain and add a randomly sampled square hole, whose borders are considered to be the inner boundary $\partial\Omega_1$. The size of the hole is sampled from the uniform distribution $U(0.05, 0.25)^2$, and its mean position is sampled from $U(0.2, 0.8)^2$. We add the closest distance to the inner boundary as an additional node feature.

B.2 Poisson's Equation

The weak formulation of the considered Poisson problem is given as

$$\int_{\Omega} \nabla u(\mathbf{x}) \cdot \nabla v(\mathbf{x}) \, d\mathbf{x} = \int_{\Omega} f(\mathbf{x})v(\mathbf{x}) \, d\mathbf{x} \quad \forall v.$$

Here, $f(\mathbf{x}) : \Omega \rightarrow \mathbb{R}$ denotes the load function and $v(\mathbf{x})$ the test function. In addition to the weak formulation, the solution must be zero on the boundary $\partial\Omega$ of the domain Ω . We model Poisson's Equation on L-shaped domains Ω , using a rectangular cutoff whose lower left corner is sampled from $p_0 \sim U(0.2, 0.95)^2$, resulting in a domain $\Omega = (0, 1)^2 \setminus (p_0 \times (1, 1))$. On this domain, we sample a Gaussian Mixture Model with 3 components. The mean of each component is sampled from $U(0.1, 0.9)^2$, using rejection sampling to ensure that all means lie within the domain. The components' covariances are determined by first drawing diagonal covariances, where each dimension is drawn independently from a log-uniform distribution $\exp(U(\log(0.0003), 0.003))$. The diagonal covariances are then rotated by a random angle in $U(0, 180)$ to produce Gaussians with a full covariance matrix. The component weights are drawn from the distribution $\exp(N(0, 1)) + 1$ and subsequently normalized, where the 1 in the end is used to ensure that all components have relevant weight. Here, the evaluation of the load function f at the respective face midpoint is added as a node feature.

B.3 Stokes flow

Let $\mathbf{u}(\mathbf{x})$ be the velocity field and $p(\mathbf{x})$ the pressure field. We consider a Stokes flow of a fluid through a channel. Therefore, we seek a solution \mathbf{u} and p , which satisfy the weak formulation of the Stokes flow without a forcing term

$$\begin{aligned} \nu \int_{\Omega} \nabla \mathbf{v} \cdot \nabla \mathbf{u} \, d\mathbf{x} - \int_{\Omega} (\nabla \cdot \mathbf{v})p \, d\mathbf{x} &= 0 \quad \forall \mathbf{v} \\ \int_{\Omega} (\nabla \cdot \mathbf{u})q \, d\mathbf{x} &= 0 \quad \forall q, \end{aligned}$$

wherein $\mathbf{v}(\mathbf{x})$ and $q(\mathbf{x})$ denote the test functions [89]. In addition, we assume a no-slip condition $\mathbf{u} = \mathbf{0}$ at both the top and bottom of the channel, and an inlet-profile defined as

$$\mathbf{u}(x = 0, y) = u_p y(1 - y) + \sin(\varphi + 2\pi y).$$

At the outlet, the gradient of velocity $\nabla \mathbf{u} = \mathbf{0}$ is set to zero. For stability purposes, we use P_1/P_2 Taylor-Hood-elements, i.e., quadratic shape functions for the velocity and linear shape functions for the pressure [88]. We sample the quadratic part u_p of the velocity inlet from a log-uniform distribution $\exp(U(\log(0.5), 2))$. The domains are a class of trapezoids that we derive from the unit square by randomly choosing 2 of the 4 vertices and adding a random inward-facing y offset drawn from $U(0, 0.45)$ to these points. The resulting trapezoid is subsequently normalized to lie in $(0, 1)^2$. We add the parabolic part of the inlet velocity of the current PDE as a global feature. We optimize the meshes for the prediction of the velocity norm and use linear shape functions for the numerical error approximation in 2 for simplicity.

B.4 Linear Elasticity

We are looking for the steady-state deformation of a solid under stress, due to displacements at the boundary of the part $\partial\Omega$. Here, we are interested in both the norm of the deformation and the norm of the stress. The weak formulation of the considered problem on the domain Ω without body forces is given as [90]

$$\int_{\Omega} \boldsymbol{\sigma}(\boldsymbol{\varepsilon}(\mathbf{u})) : \boldsymbol{\varepsilon}(\mathbf{v}) \, d\mathbf{x} = 0.$$

Here, $\mathbf{u}(\mathbf{x})$ is the displacement field, $\mathbf{v}(\mathbf{x})$ is the test function, and $\boldsymbol{\varepsilon}(\mathbf{u}) = \frac{1}{2}(\nabla \mathbf{u} + (\nabla \mathbf{u})^\top)$ is the strain tensor. $\boldsymbol{\sigma}(\boldsymbol{\varepsilon})$ is the stress tensor, which is given as $\boldsymbol{\sigma}(\boldsymbol{\varepsilon}) = 2\mu\boldsymbol{\varepsilon} + \lambda\text{tr}(\boldsymbol{\varepsilon})\mathbf{I}$ in a linear-elastic and isotropic case. The Lamé parameters $\lambda = \frac{E\nu}{(1+\nu)(1-2\nu)}$ and $\mu = \frac{E}{2(1+\nu)}$ can be calculated with the problem specific Young's modulus $E = 1$ and the Poisson ratio $\nu = 0.3$. The displacement

$\mathbf{u}(x = 0, y) = \mathbf{u}_0$ on the left side of the boundary is specified by a task-dependent parameter \mathbf{u}_0 , whereas the displacement $\mathbf{u}(x = L, y) = 0$ is set to zero on the right boundary. The stress $\boldsymbol{\sigma} \cdot \mathbf{n} = \mathbf{0}$ is zero normal to the boundary at both the top and bottom of the part. We use the same class of L-shaped domains as in the Poisson problem in Section B.2 and set u_P by drawing a random angle from $U[0, \pi]$ to pull on the domain from different angles, and add random magnitude from $U(0.2, 0.8)$. We add the task-dependent displacement u_P as a global feature. We are interested in the norm of the displacement field u and the resulting Von-Mises stress, giving us a 2-dimensional objective. We weight both dimensions equally in the reward.

B.5 Non-stationary Heat Diffusion

We consider a non-stationary thermal diffusion problem defined by the weak formulation

$$\int_{\Omega} \frac{\partial u}{\partial t} \, d\mathbf{x} + \int_{\Omega} a \nabla u \cdot \nabla v \, d\mathbf{x} = \int_{\Omega} f v \, d\mathbf{x} \quad \forall v,$$

wherein u denotes the temperature, v the test function, a the thermal diffusivity and f a heat distribution, given as

$$f = q \exp(-100((x - x_p(\tau)) + (y - y_p(\tau)))).$$

The position of the maximum heat entry $\mathbf{p}_{\tau}(\tau) = (x_p(\tau), y_p(\tau))$ is changing over time, while its magnitude is scaled by a factor q . The temperature $u \in \partial\Omega$ is set to zero on all boundaries. For the time-integration, the implicit euler method is applied. We use a total of $\tau_{\max} = 20$ time steps in $\{0.5, \dots, 10\}$, a scaling factor of $q = 1000$ and a diffusivity $a = 0.001$. The position of the heat source at step τ is linearly interpolated as $\mathbf{p}_{\tau} = \mathbf{p}_0 + \frac{\tau}{\tau_{\max}}(\mathbf{p}_{\tau_{\max}} - \mathbf{p}_0)$, where the start and goal positions \mathbf{p}_0 and $\mathbf{p}_{\tau_{\max}}$ are randomly drawn from the domain. To create our domains, we start with 10 points that are equidistantly placed on a circle with center $(0.5, 0.5)$ and radius 0.4. Each point is distorted by a random value drawn from $U(-0.2, 0.2)^2$. We then normalize the resulting points to be in $(0, 1)^2$ and calculate the convex hull. The result is a family of convex polygons with up to 10 vertices. We measure the error of the final simulation step, and provide the distance to the start and end position of the heat source as additional node features.

C Further Experiments

C.1 Experiment Details

All experiments are repeated for $n = 10$ random seeds with randomized PDEs and network parameters. All PDEs are normalized to be in $(0, 1)^2$. We train all policies on 100 training PDEs and evaluate the resulting final policies on 100 different evaluation PDEs that we keep consistent across random seeds for better comparability. All experiments are run for up to 3 days on 8 cores of an Intel Xeon Platinum 8358 CPU.

In terms of total compute, we train 4 different learned methods, namely the 3 RL baselines and our method, on 5 separate tasks. Each experiment is repeated for 10 different target mesh resolutions and 10 repetitions, resulting in $5 \cdot 4 \cdot 10 \cdot 10 = 2000$ main experiments, each of which is run for up to 3 days. Additionally, we use a similar amount of compute for the combined ablations, preliminary experiments and error-based heuristics.

For practical purposes, we add an element threshold β_{\max} in our environments, and terminate an episode with a large negative reward when this threshold is exceeded.

C.2 Maximum Reward

Equation 3 scales the reduction in error of each element by its area. This modification encourages the policy to focus on smaller elements, effectively shifting the objective from an reduction in average error across the mesh to a minimization of error densities.

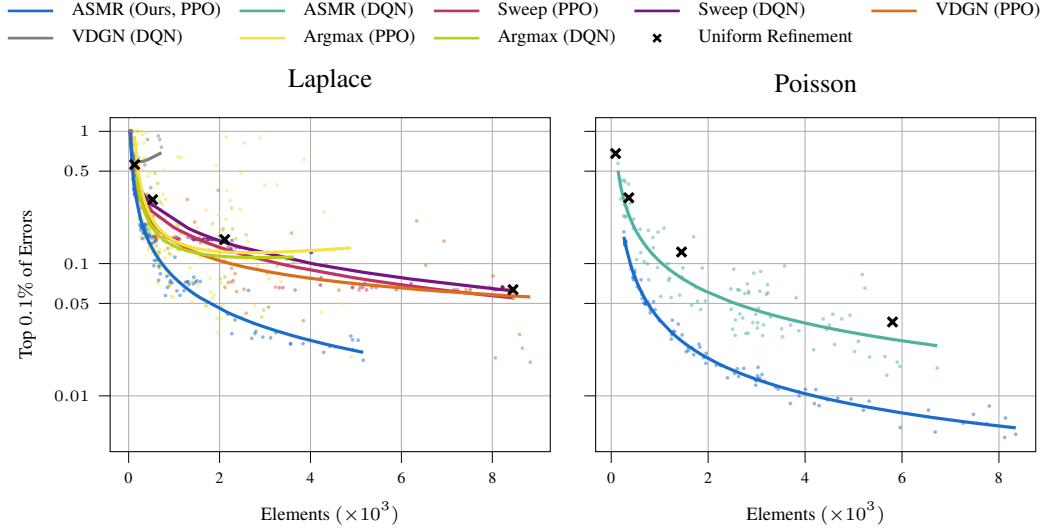


Figure 8: Pareto plot of normalized Top 0.1 % of errors and number of final mesh elements for (Left) PPO and DQN for all RL baselines on the Laplace equation and (Right) PPO and DQN for ASMR on the Poisson task. PPO generally results in better performance, with the exception of *Argmax*, which is slightly better when using DQN. The performance of *Argmax* is likely a result of the comparatively simple action space of only refining a single element per environment step.

An alternate way to phrase this objective is to make the reward depend on the reduction in maximum error per element. For this, we modify the error estimate per element of Equation 2 to read

$$\hat{\text{err}}(\Omega_i^t) \approx \max_{\Omega_m^* \subseteq \Omega_i^t} \left| u_{\Omega^*}(p_{\Omega_m^*}) - u_{\Omega^t}(p_{\Omega_m^*}) \right|,$$

and subsequently drop the area scaling and replace the sum in Equation 3 with a maximum, i.e.,

$$\mathbf{r}'(\Omega_i^t) := \left(\text{err}(\Omega_i^t) - \max_j \mathbf{M}_{i,j}^t \text{err}(\Omega_j^{t+1}) \right) - \alpha \left(\sum_j \mathbf{M}_{i,j}^t - 1 \right).$$

While conceptually simpler than our reward formulation, evaluating the decrease in maximum error optimizes only this objective, and may result in degenerate meshes when looking at the overall error. Figure 6 compares this alternate reward formulation to that of ASMR. We find that this reward generally performs a bit better than the variant of Equation 3 on the Top 0.1 % of errors, and a bit worse on the mean remaining error. Overall, both reward formulations work roughly equally well. We thus use the reward of Equation 3 for simplicity and easier comparison with the baseline methods.

D Extended Results

D.1 Baseline Algorithms

The left of Figure 8 shows results for the RL baseline methods for both PPO and DQN as the RL backbone. We find that PPO performs better for *VDBG* and *Sweep*, while DQN seems to be better for *Argmax*. For the PPO variant of *VDBG*, we factorize the value function instead of the Q-function, i.e., we define the value function of the full mesh as the sum of value functions of the individual mesh elements.

D.2 Ablations.

Proximal Policy Optimization and Deep Q-Networks. The right of Figure 8 compares ASMR with PPO and DQN as the RL algorithms. We find that a using a mean instead of a sum for the agent mapping of the targets of the Q-values increases training stability, and thus use it for the DQN

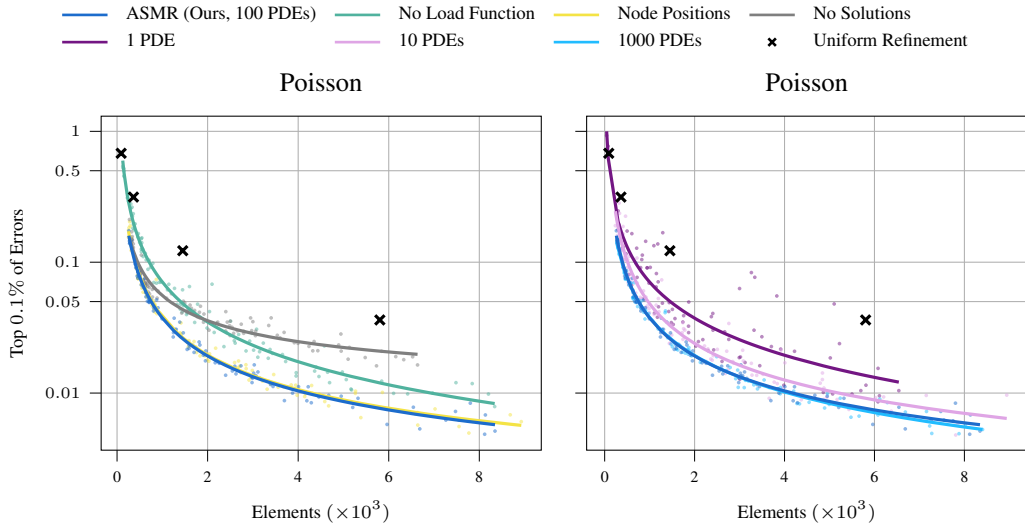


Figure 9: Pareto plot of normalized Top 0.1 % of errors and number of final mesh elements for Poisson’s Equation. (Left) Omitting either the solution or evaluation of the load function per element significantly decreases the performance of our approach. Adding explicit node positions is slightly detrimental to the performance, likely because it causes the observation to no longer be equivariant to e.g., reflection. (Right) Performance is reduced for fewer training PDEs, but stabilizes around 100 PDEs. Interestingly, ASMR achieves acceptable performance when using a single training PDE, which is likely a result of our spatial problem formulation.

experiments with ASMR. However, the PPO variant still performs significantly better than the DQN one. As such, we use PPO as the RL algorithm for ASMR for all other experiments.

Node Features. ASMR utilizes both task-dependent information, such as the evaluation of the load function for Poisson’s Equation, and the local solution $u(x)$ per mesh element as part of its observation graph. Here, we experiment how the performance is affected if either of these features is omitted. Additionally, we consider a variant where we include explicit (x, y) positions of each element midpoint as node features. The results are shown on the left of Figure 9. We find that both the task-dependent features and the solution are important for the performance of our approach. *Not* adding positional features slightly improves performance, presumably because the features assign a fixed position to each mesh element, causing the observation graph to no longer be equivariant to rotation, translation and reflection. Interestingly, ASMR provides reasonable refinements even without solution information, suggesting that the RL algorithm is able to detect relevant regions of the PDE from just an encoding of the domain and the boundary conditions.

Number of Training PDEs Since calculating the fine-grained reference Ω^* is slow for large meshes and complex tasks, we want to minimize the number of unique PDEs that we need during training. We use 100 PDEs in our other experiments, and additionally visualize results for 1, 10 and 1000 training PDEs on the right of Figure 9. We find that fewer than 100 PDEs lead to less stable and reliable results, and that there is only a minor advantage in using 1000 PDEs compared to our 100. Noticeably, a single training PDE results in acceptable refinements in most cases, which hints at significant generalization capabilities that are likely due to our spatial treatment of the underlying task.

D.3 Runtime comparison.

We compare the wallclock-time of our approach with that of directly computing the fine-grained uniform mesh Ω^* . For our approach, we measure the cumulative time of creating an initial coarse mesh, and then iteratively solving the problem on this mesh, computing the resulting observation graph, feeding the observation graph to the policy to obtain actions, and using these actions to refine the mesh a total of $T = 6$ times. For the uniform mesh, we simply measure the time it takes to refine the coarse mesh 6 times and to subsequently solve the problem on the resulting mesh. We use a

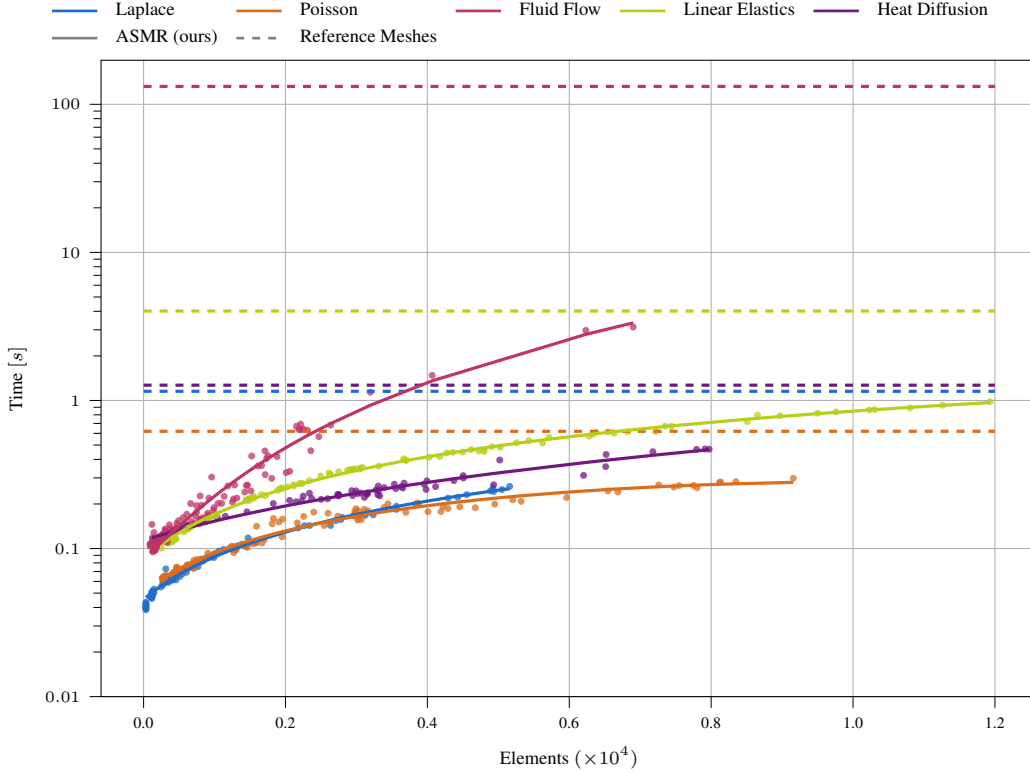


Figure 10: Wallclock-time (in seconds) of ASMR for different numbers of elements compared to the uniform reference Ω^* . The dotted lines represent the wallclock-time of creating and solving Ω^* , while the full lines represent a quadratic regression of the wallclock-time of our method for different numbers of final elements. On average, Ω^* contains about 10^5 elements, with concrete numbers varying depending on the domain. Our approach is significantly faster than the reference for all tasks.

single 8-Core AMD Ryzen 7 3700X Processor for all measurements. Figure 10 shows the results for all considered tasks. We find that our approach is always significantly faster than computing the fine-grained mesh despite the comparatively large computational overhead. Further, the final resolution of the computed meshes trades off the wallclock-time of the method, meaning that ASMR can be trained to generate coarser or finer meshes depending on task-specific computational budgets. Notably, for the Navier Stokes equations, which use P_1/P_2 Taylor-Hood-elements, our method is more than 30 times faster than Ω^* even for highly refined final meshes.

D.4 Generalization capabilities.

We qualitatively test the generalization capabilities of our method by employing it for different Poisson tasks. For this, we consider the 4 different domain types used in throughout the main experiments, plus a simple rectangular domain $\Omega = (0, 1)^2$. We sample 3 random domains from each class, and use Gaussian Mixture Model load functions with 1, 3 and 5 components respectively. Figure 11 shows refinements of an ASMR policy with $\alpha = 0.0075$ for the resulting 3×5 problems. We find that ASMR generalizes across all domains and load functions, which is likely a result of the Swarm RL setting, where each mesh element is governed by its own agent.

D.5 Target Mesh Resolutions

All RL methods use some parameter to control the number of target elements of the final refined mesh. ASMR and *VDGN* use an element penalty α , *Sweep* uses a budget N_{\max} , and *Argmax* different numbers of rollout steps T . We visualize the effect of different target resolutions in Figure 12. The results indicate that ASMR provides meshes with consistent numbers of elements for a given target resolution, while the other RL methods produce meshes with different numbers of elements for the

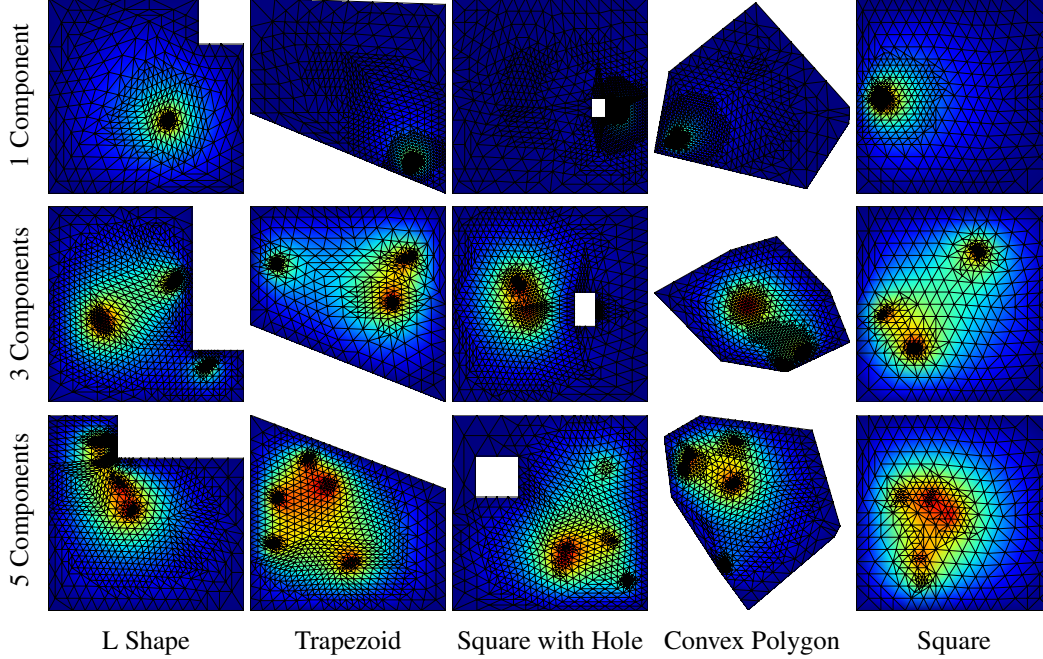


Figure 11: Final refined meshes of ASMR for different domains and Poisson’s equation with a Gaussian Mixture Model load with 1, 3 and 5 components. Even though ASMR is only trained on L-shaped domains with 3 components in the load function, it generalizes to different domains as well as more and less complex loads.

same or similar target resolutions. The concrete target resolution parameters used for our experiments are found in Table 1.

D.6 Alternate Error Metrics

Section 5 evaluates all approaches on the normalized average of the Top 0.1 % of errors of the numerical integration. The left of Figure 13 instead shows the error of the Top 5 % of integration points for the Poisson task. We find that the results similar to that of Figure 4, i.e., that approaches that perform well on the highest 0.1 % of errors also generally show good results on a larger percentage of errors.

Using the notation of Section 3, we can also measure the mean remaining error of the final refinement Ω^T compared to the reference Ω^* via its normalized mean error, i.e., as

$$\frac{\sum_r \text{Area}(\Omega_m^*) |u_{\Omega^*}(p_{\Omega_m^*}) - u_{\Omega^T}(p_{\Omega_m^*})|}{\sum_r \text{Area}(\Omega_m^*) |u_{\Omega^*}(p_{\Omega_m^*}) - u_{\Omega^0}(p_{\Omega_m^*})|}.$$

This metric can be seen as a Top 100 % error, except that each integration point is additionally scaled with the area of its corresponding reference element. The right of Figure 13 shows results for this linear error for the Poisson equation. Figure 14 displays results for the Laplace equation and the Stokes flow, and results for the linear elasticity and heat diffusion tasks are shown in Figure 15. The general trends for the linear errors are consistent with the Top 0.1 % errors of Section 5. Since this metric focuses on the mean instead of the maximum error, the *Local Oracle* performs better than on the Top 0.1 % metric, reaching or surpassing the performance of the *Local Maximum Oracle* on most tasks. Still, both local oracle heuristics seem to perform different and in some cases sub-optimal, likely due to global dependencies in the PDEs and due to the remesher enforcing a conforming solution. ASMR provides accurate refinements that optimize both the Top 0.1 % and the remaining linear error on most tasks. For e.g., the linear elasticity task, the refinements provided by ASMR significantly outperform both error-based oracle heuristics, likely because this task has global dependencies that can be learned by the RL algorithm, but are ignored by the local heuristics. For the

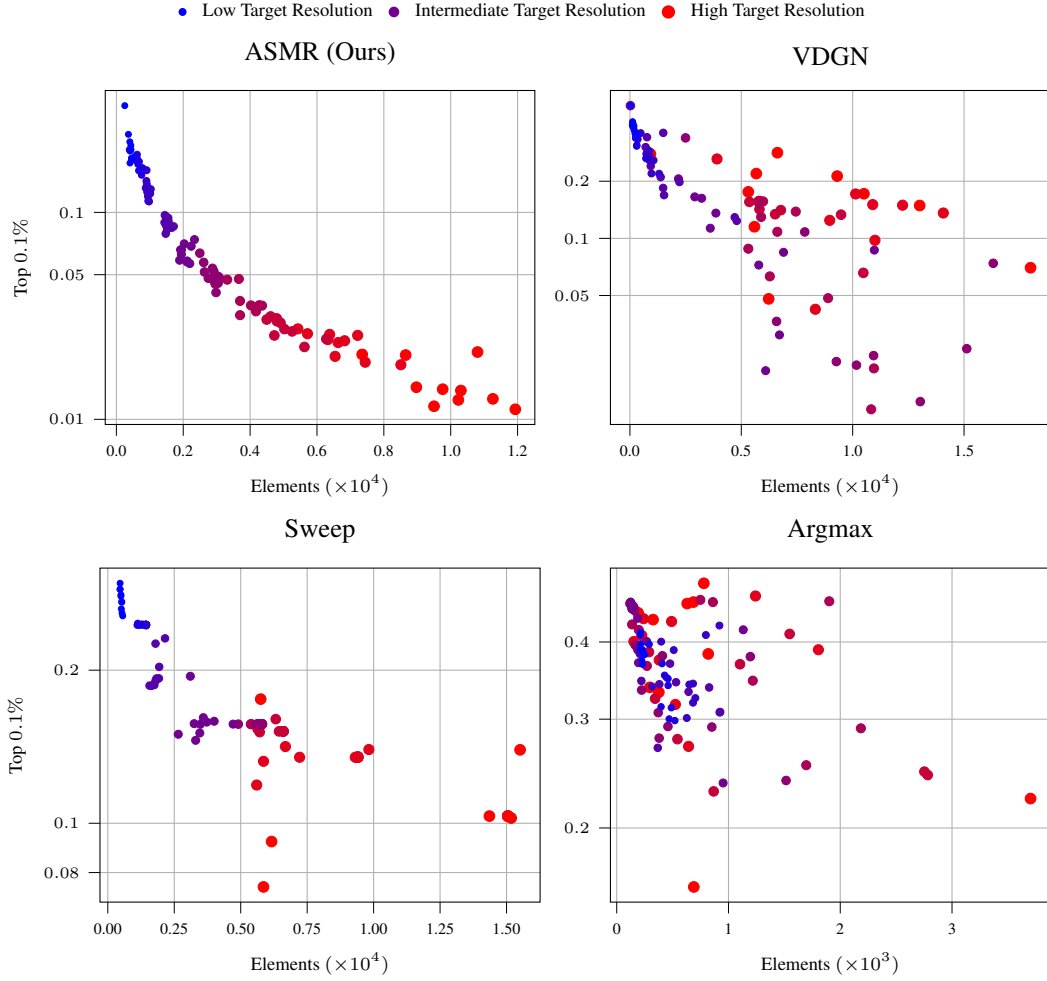


Figure 12: Pareto plot of normalized Top 0.1 % of errors and number of final mesh elements for the linear elasticity task for all RL methods. Small blue dots indicate a random seed trained on a coarse target mesh resolution, which corresponds to large element penalties α for ASMR and *VDBG*, a small budget N_{\max} for *Sweep* and a low number of rollout steps T for *Argmax*. Large red dots correspond to a finer target mesh resolution, and the purple dots interpolate between the two. Details on the target resolution parameters are found in Table 1. We find that ASMR provides high-quality refinements with consistent numbers of final mesh elements for any given target resolution, whereas the other methods yield widely different results for similar target resolutions when trained on different random seeds.

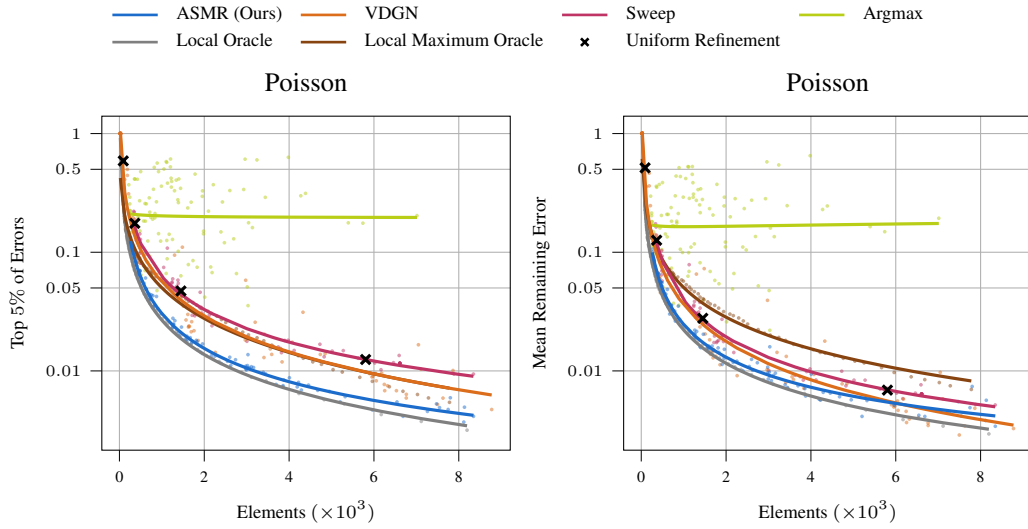


Figure 13: Pareto plot of the normalized (Left) Top 5 % of errors and (Right) mean remaining error and number of final mesh elements for the Poisson equation. The results are similar to the Top 0.1 % of errors as seen in Figure 4. The Top 5 % metric interpolates between the Top 0.1 % and the mean remaining error. We find that the performance of the *Local Maximum Oracle* degrades when evaluating more integration points, likely because it only focuses on the maximum error of each element by construction. ASMR provides refinements that perform well on all considered metrics.

Stokes flow, a simple uniform refinement seems to be sufficient to reduce the mean remaining error, suggesting that the distribution of total error mass is comparatively homogeneous. The behavior of different variants of our reward function on this metric are provided in Figure 6.

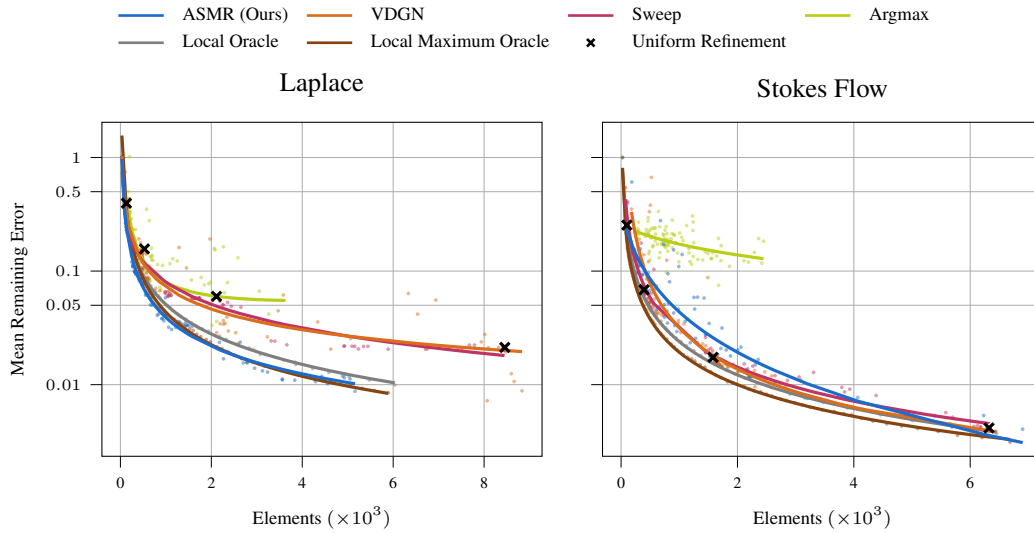


Figure 14: Pareto plot of the normalized mean remaining error for (Left) the Laplace equation and (Right) the Stokes flow. The mean remaining error weights areas with high error less when compared to the Top 0.1% of errors. As a result, both the uniform refinement and the methods that produce more uniform meshes, such as *Sweep*, perform better on this metric. For the Stokes flow task, the mesh must be relatively uniform across the full length of the domain to reduce the total error mass, which likely causes the uniform refinements to be comparatively good.

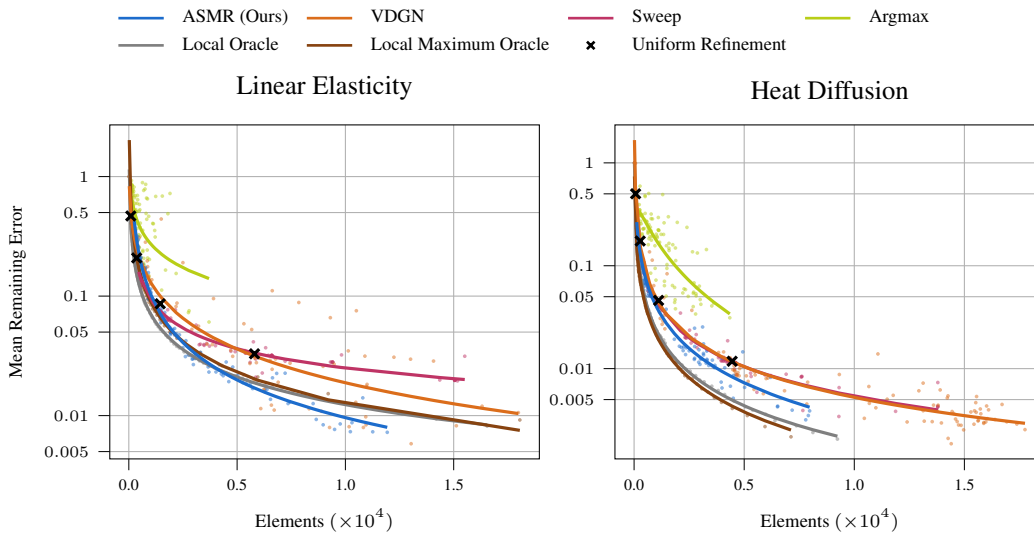


Figure 15: Pareto plot of the normalized mean remaining error for (Left) the linear elasticity and (Right) the heat diffusion task. The mean remaining error weights areas with high error less when compared to the Top 0.1% of errors. Thus, uniform refinements and methods that produce uniform refinements generally perform better on this metric. Interestingly, ASMR outperforms both the *Local Oracle* and the *Local Maximum Oracle* on the linear elasticity task, likely because the task has global dependencies that are respected by our RL framework, but are ignored by the local heuristics.

E Hyperparameters

E.1 General Hyperparameters

We use the same hyperparameters across all methods and environments unless mentioned otherwise.

PPO. We largely follow the suggestions of [91] for our PPO parameters. We train each PPO policy for a total of 800 iterations. In each iteration, the algorithm samples 256 environment transitions and then trains on them for 5 epochs with a batch size of 32. The value function loss is multiplied with a factor of 0.5 and we clip the gradient norm to 0.5. The policy and value function clip ranges are chosen to be 0.2. We normalize the observations with a running mean and standard deviation. The discount factor is $\gamma = 0.99$ and advantages are estimated via Generalized Advantage Estimate [92] with $\lambda = 0.95$. Similar to how we average local and global returns in Equation 4, we compute an agent’s advantage by taking a middle ground between local and global advantages. For a given agent, we average its own local advantage and the average local advantages of all other agents of the same mesh.

DQN. For DQN-based approaches, we instead train for $24 * 800 = 19200$ steps, where each step consists of executing an environment transition and then drawing a batch of samples 32 samples from the replay buffer for a single gradient update. Since every environment transition describes a full refinement step, including a mesh and its solution, we keep a total of 5000 transitions in the replay buffer. We additionally draw 500 initial random replay buffer samples before the first training step. During training, we draw actions using a Boltzmann distribution over the predicted Q-values per agent, where we linearly decrease the temperature of the distribution from 10 to 0.01 in the first 9600 steps. We find that this action selection strategy leads to more correlated actions when compared to an epsilon greedy action sampling, which stabilizes the training for our iterative mesh refinement problems. We update the target networks using Polyak averaging at a rate of 0.99 per step. Further, we follow previous work [93] and combine a number of common improvements for DQNs, namely double Q-learning [94], dueling Q-networks [95] and prioritized experience replay [96].

Neural Networks. All networks are implemented in PyTorch [97] and trained using the ADAM optimizer [98] with a learning rate of $3.0e-4$ unless mentioned otherwise. All MLPs use 2 hidden layers and a latent dimension of 32. We use separate MPNs for the policy and the value function. Each MPN consists of 2 message passing steps, where each update function is represented as an MLP with *LeakyReLU* activation functions. The policy and value function heads are additional MLPs with *tanh* activation functions acting on the final latent node features of the MPN. All message aggregations \oplus are mean aggregations. Additionally, we apply Layer Normalization [99] and Residual Connections [100] independently for the node, edge and global features after each message passing step.

E.2 Baseline-Specific Parameters

To accommodate the step-wise nature of *Argmax* and *Sweep*, we increase the size of their replay buffer to 10000 when using DQN. For *Argmax*, we use a maximum refinement depth of 10 refinements per element to avoid numerical instabilities during simulation, skipping actions that try to refine elements that have been refined too often. We consider environment sequences of up to $T = 400$ steps since the method marks only one element at a time. Due to the computational demand of this method, we only evaluate it on 10 instead of 100 evaluation PDEs. For *Sweep*, the agent is placed on a random mesh element for each training step and may decide not to refine this element, resulting in no change in the mesh. Here, we follow the proposed hyperparameters for this approach and train each rollout for 200 steps. As this approach is based on purely local agents, we adapt our input features per element to consist of our regular node features, the global resource budget proposed by the authors, the mean solution and area of the element’s neighbors and the average distance to them. The global budget is controlled via a maximum number of elements N_{\max} , allowing to get refinements of different granularity. To accommodate for less overall changes in the mesh, we increase the number of environment transitions of PPO to 512, and the number of DQN steps to $96 * 800 = 76800$. Finally, we use a learning rate of $1.0e-5$ instead of $3.0e-4$ for the DQN variant of *VDPN* to stabilize its training.

E.3 Refinement Hyperparameters

The AMR methods considered in this work use different parameters to control the granularity of the final refined mesh. ASMR and VDG N use an element penalty α , while Sweep considers an element budget N_{\max} . Similarly, Argmax varies the number of rollout steps T , and the Local Oracle and Local Maximum Oracle use different error thresholds θ . For each method and task, we choose 10 different values for the refinement parameter that showcase a wide range of final mesh resolutions. Table 1 lists the different ranges for these parameters for the different tasks. For stability purposes, we set a maximum number of 20000 elements for all experiments except for the Sweep baseline, as this baseline uses its own element budget instead. If this number is surpassed, a constant penalty of 1000 is subtracted from the reward and the episode terminates early.

Table 1: Ranges for the different refinement hyperparameters for all tasks. ASMR and VDG N apply an element penalty α , but only ASMR scales the area of each element with its area in Equation 3. Sweep uses an element budget N_{\max} . Argmax varies the number of rollout steps T , and the Local Oracle and Local Maximum Oracle make use of different error thresholds θ .

Method	Task				
	Laplace	Poisson	Stokes Flow	Lin. Elasticity	Diffusion
ASMR (α)	[0.01, 0.3]	[0.002, 0.1]	[0.006, 0.15]	[0.01, 0.15]	[0.003, 0.3]
VDG N (α)	[2e-5, 5e-2]	[2e-5, 5e-2]	[3e-4, 5e-3]	[1e-5, 1e-2]	[5e-6, 5e-3]
Sweep (N_{\max})	[200, 3000]	[400, 5000]	[200, 3000]	[500, 6000]	[400, 5000]
Argmax (T)	[25, 400]	[25, 400]	[25, 400]	[25, 400]	[25, 400]
Local Oracle (θ)	[0.25, 1.00]	[0.1, 1.0]	[0.16, 1.0]	[0.02, 1.0]	[0.03, 1.0]
L. Max. Oracle (θ)	[0.20, 1.0]	[0.2, 1.0]	[0.1, 1.0]	[0.01, 1.0]	[0.02, 1.0]

F Visualizations

We provide additional visualizations for our method on all tasks, and for all methods on the Poisson task. All visualizations show the final refined mesh of the respective method for 5 different refinement levels on 3 randomly selected PDEs. For the RL methods, all policies are taken from the first repetition of the 10 random seeds conducted for the respective experiment.

F.1 ASMR Refinements

We visualize exemplary refinements of ASMR policies for all considered tasks. The visualizations are given in Figure 16 (Laplace’s equation), Figure 17 (Poisson’s equation), Figure 18 (Stokes equation), Figure 19 (Linear Elasticity), and Figure 20 (Heat Diffusion). Across all tasks, ASMR is able to provide highly accurate refinements for different numbers of total elements.

F.2 Baseline Comparisons

Figure 21 shows refinements for *Argmax* for different total timesteps T , Figure 22 presents *VDGN* with different α values. Figure 23 visualizes refinements of *Sweep* for a varying number of maximum elements N_{\max} , and Figures 24 and 25 show refinements of the *Local Oracle* and *Local Maximum Oracle* for different values of the threshold θ .

The visualizations show that the RL baselines struggle to provide consistent high-quality refinements for different mesh resolutions. The *Argmax* baseline sometimes focuses on uninteresting regions of the mesh or refines the same area too often. Generally, *VDGN* performs well, but it tends not to focus enough on the interesting regions of the domain. *Sweep* provides almost uniform refinements for most PDEs and element budgets, likely as a result of the misalignment in the environment transitions between training and inference. Finally, the error-based heuristics greedily refine the elements with the largest errors of their respective metric. For the *Local Maximum Oracle*, only the areas with the highest error are repeatedly refined every step, while the *Local Oracle* refines more uniformly as it considers the total error mass per mesh element. Both behaviors lead to locally optimal refinements on their respective metric, but may cause issues for PDEs with global dependencies [87] and conforming refinements.

F.3 Element Markings

Figure 26 visualizes a full rollout of our method, including the markings of the elements after every step.

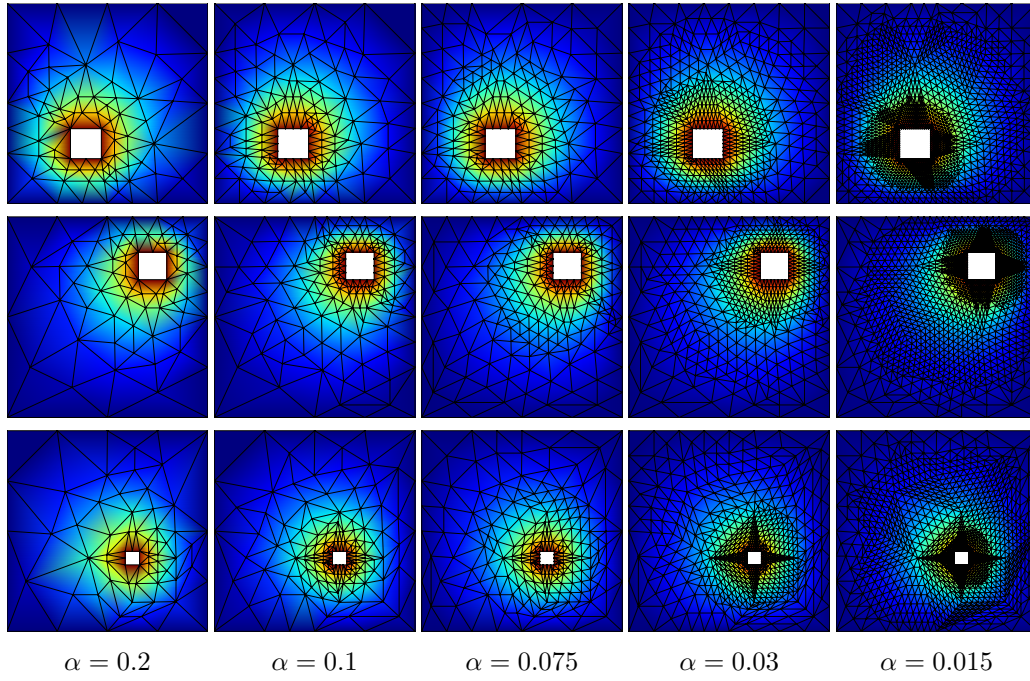


Figure 16: Final refined meshes of ASMR for randomly sampled PDEs for the Laplace equation for different element penalties α .

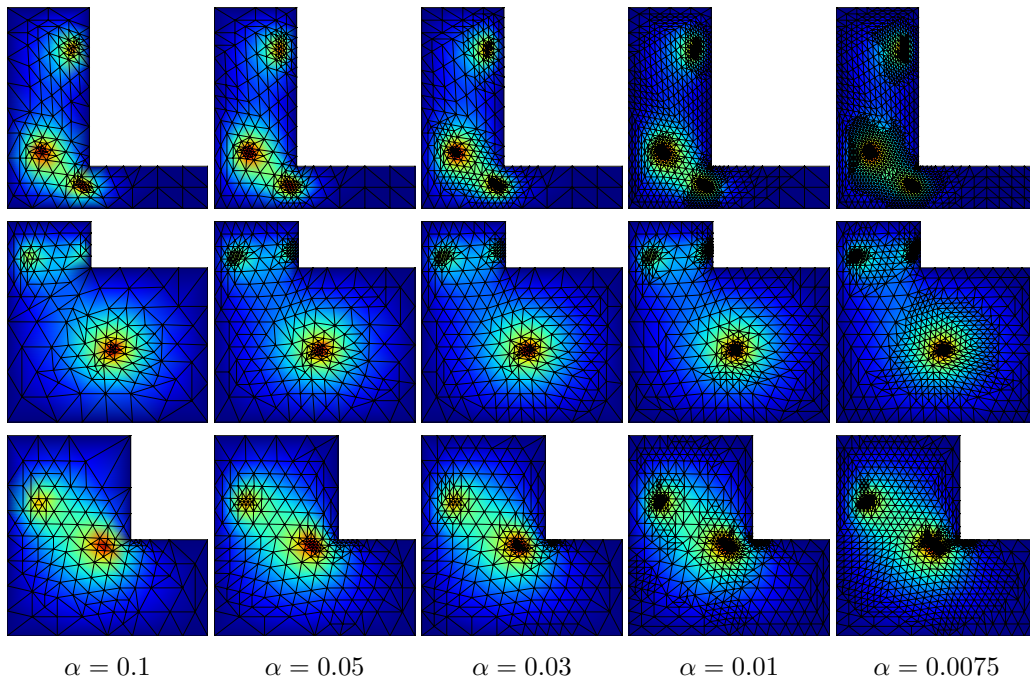


Figure 17: Final refined meshes of ASMR for randomly sampled PDEs for the Poisson equation for different element penalties α .

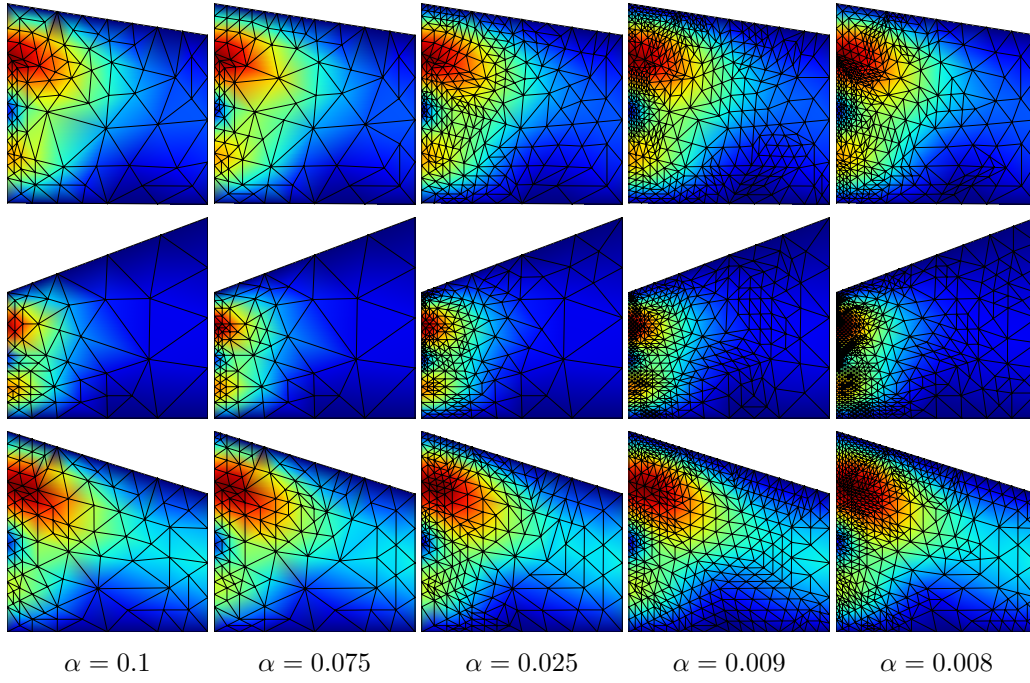


Figure 18: Final refined meshes of ASMR for randomly sampled PDEs for the Stokes flow task for different element penalties α .

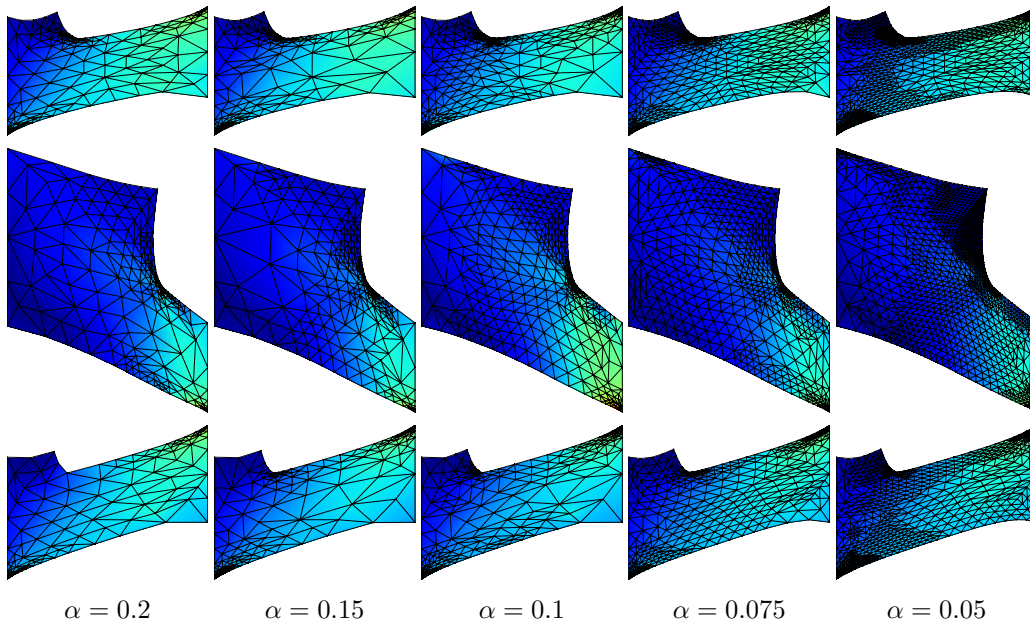


Figure 19: Final refined meshes of ASMR for randomly sampled PDEs for the linear elasticity task for different element penalties α . The visualizations show the deformed meshes, which are originally L-shaped.

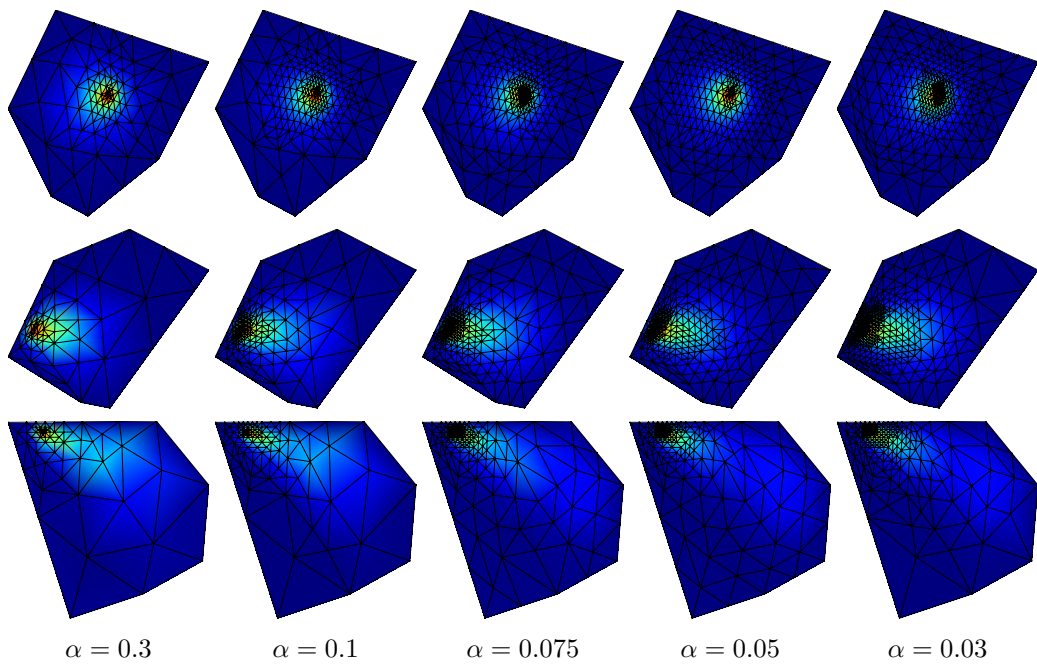


Figure 20: Final refined meshes of ASMR for randomly sampled PDEs for the non-stationary heat diffusion task for different element penalties α .

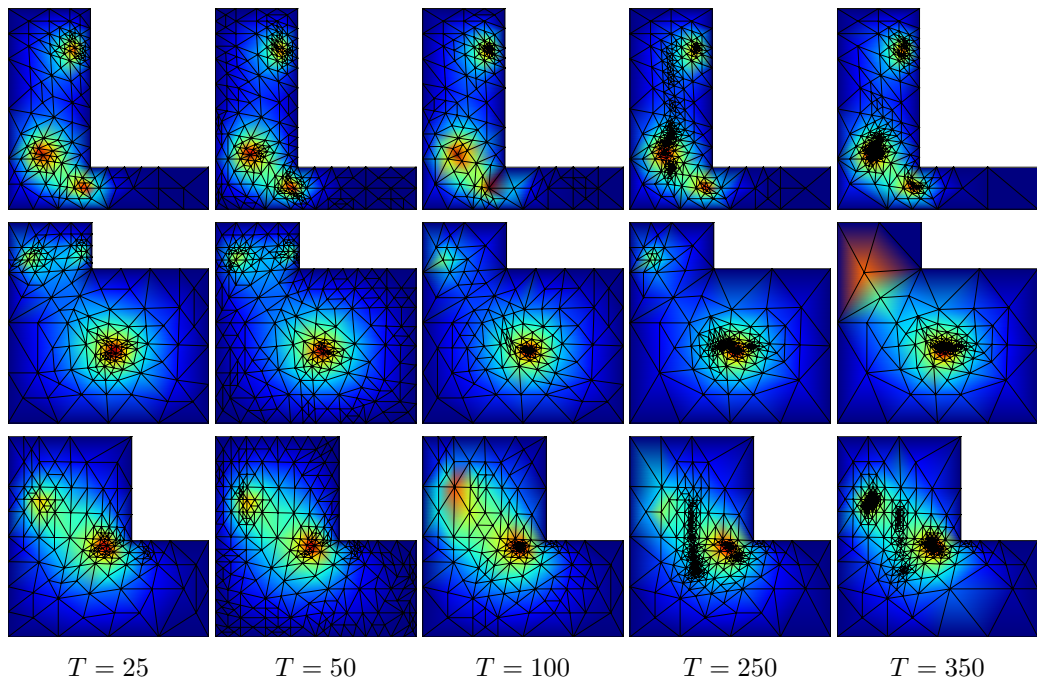


Figure 21: Final refined meshes of the *Argmax* baseline for the Poisson equation on randomly sampled PDEs for different environment rollout lengths T .

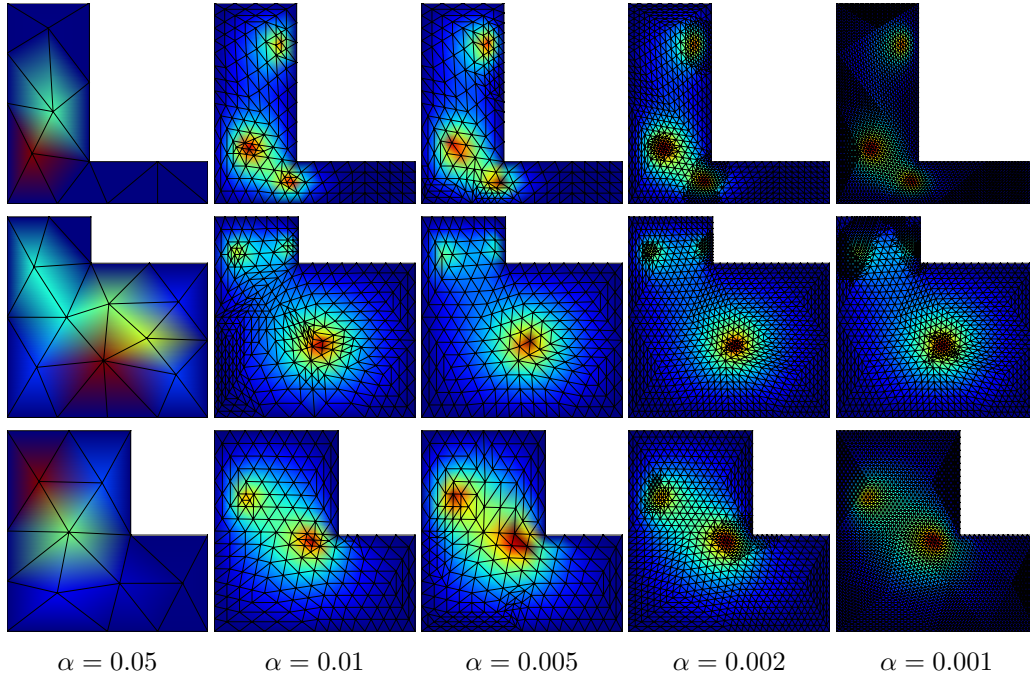


Figure 22: Final refined meshes of the *VDGn* baseline for the Poisson equation on randomly sampled PDEs for different element penalties α .

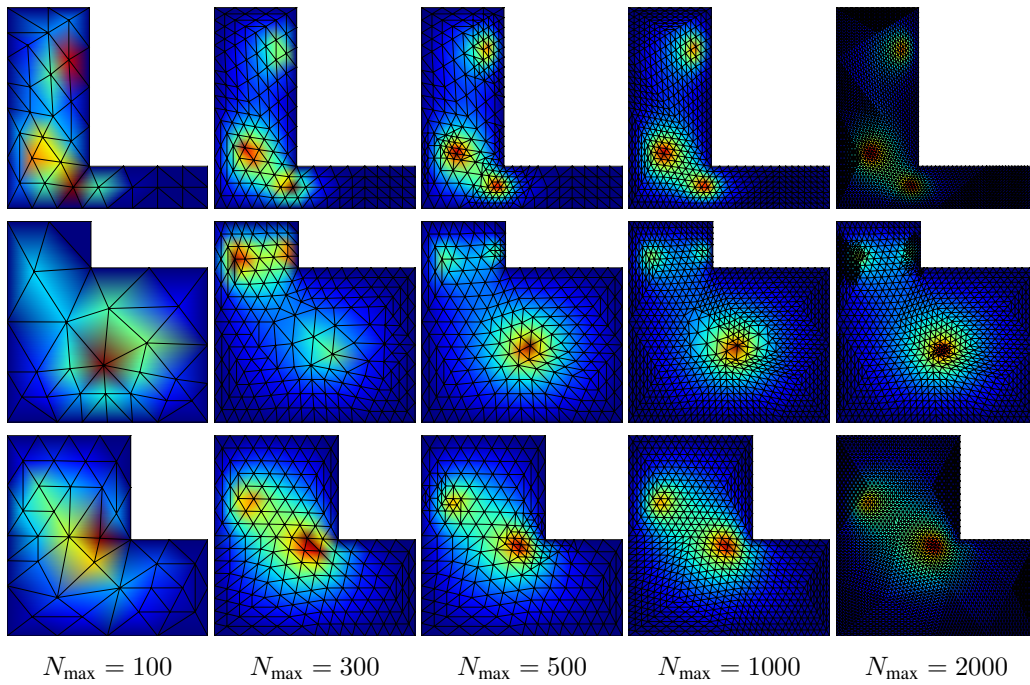


Figure 23: Final refined meshes of the *Sweep* baseline for the Poisson equation on randomly sampled PDEs for different maximum numbers of elements N_{\max} .

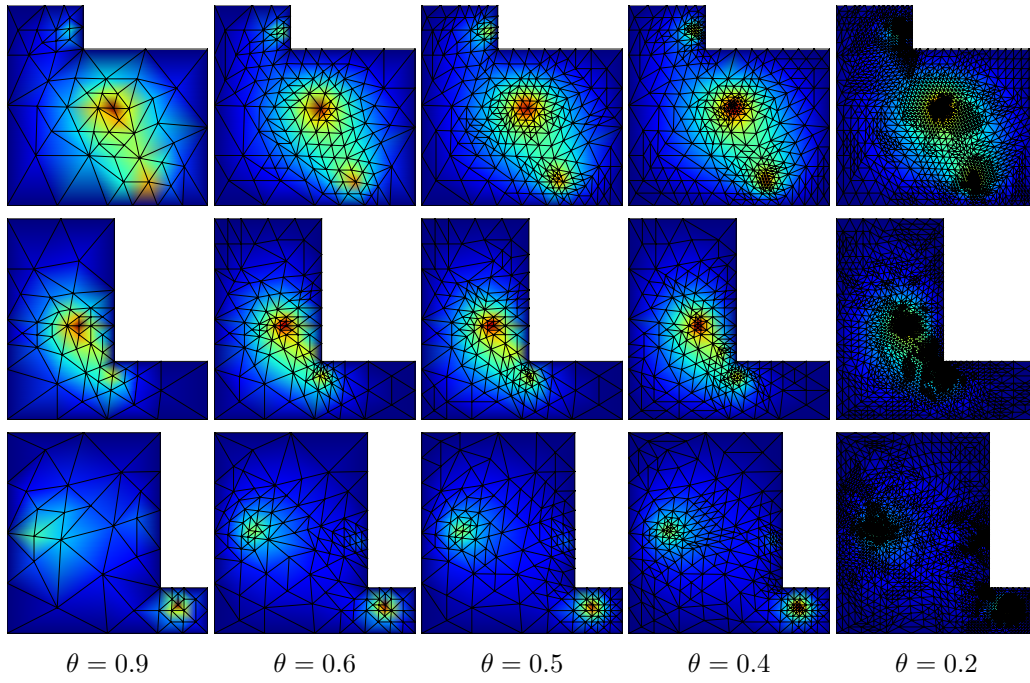


Figure 24: Final refined meshes of the *Local Oracle* baseline for the Poisson equation on randomly sampled PDEs for different error thresholds θ .

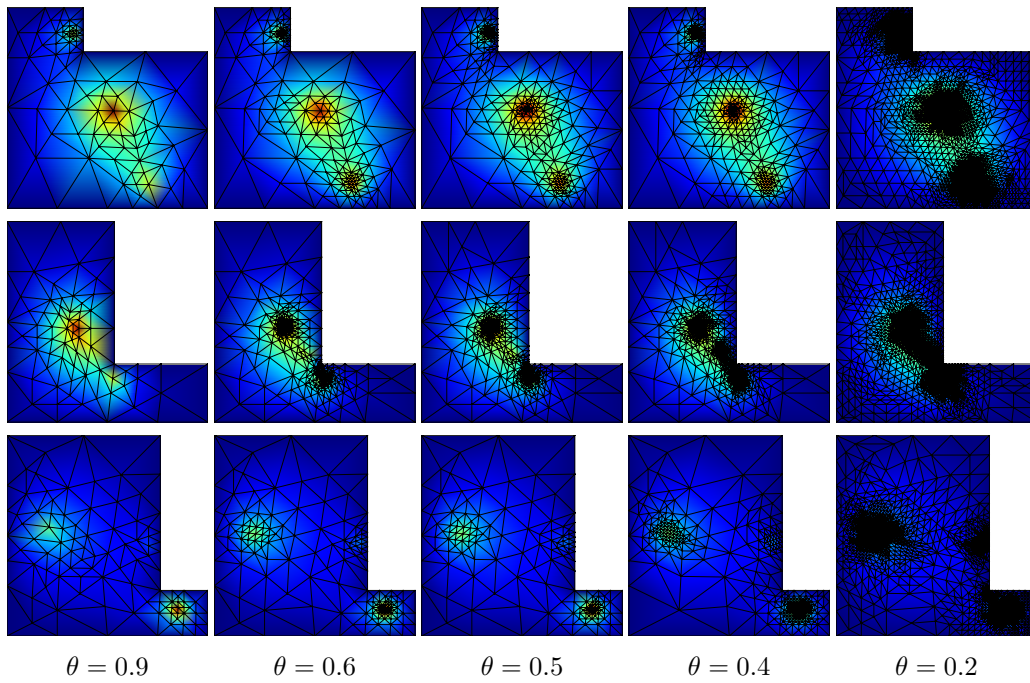


Figure 25: Final refined meshes of the *Local Maximum Oracle* baseline for the Poisson equation on randomly sampled PDEs for different error thresholds θ .

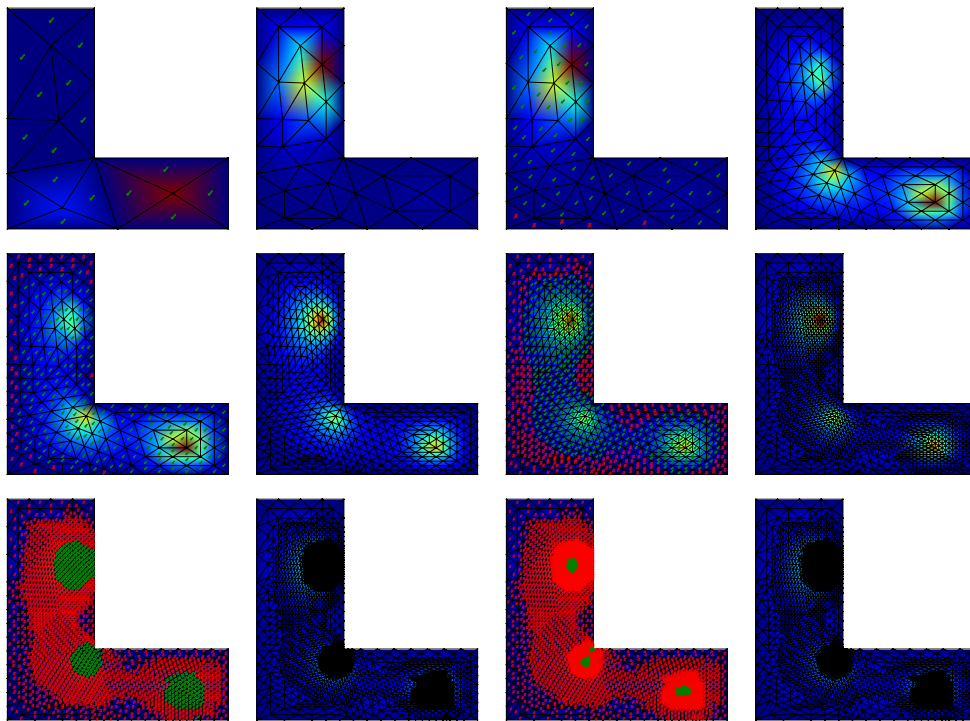


Figure 26: Visualization of a full rollout of our method on a Poisson task, including the markings of the elements after every step. The figures in the first and third row show the markings, and the second and fourth row show the resulting refined meshes.